

Stratigraphic and geochronologic investigation of the Muddy Creek Basin: Implications for the Eocene tectonic evolution of southwest Montana, USA

H.E. Thoresen^{1,†}, E.J. Cassel¹, M.E. Smith², D.F. Stockli³, and B.R. Jicha⁴

- ¹Department of Earth and Spatial Sciences, University of Idaho, Moscow, Idaho 83843, USA
- ²School of Earth and Environmental Sustainability, Northern Arizona University, Flagstaff, Arizona 86011, USA
- ³Department of Earth and Planetary Sciences, Jackson School of Geosciences, University of Texas at Austin, Austin, Texas 78712, USA

River due to uplift and doming of the south-

ern Absaroka volcanic province, resulting

in its diversion away from the Green River

⁴Department of Geoscience, University of Wisconsin–Madison, Madison, Wisconsin 53706, USA

ABSTRACT

Sedimentary basins record crustal-scale tectonic processes related to the construction and demise of orogenic belts, making them an invaluable archive for the reconstruction of the evolution of the North American Cordillera. In southwest Montana, USA, the Renova Formation, considered to locally represent the earliest accumulation following Mesozoic-Cenozoic compressional deformation, is widespread but remains poorly dated, and its origin is debated. Herein, we employed detrital zircon U-Pb and (U-Th)/ He double dating and sanidine 40Ar/39Ar geochronology in the context of decimeterscale measured stratigraphic sections in the Renova Formation of the Muddy Creek Basin to determine basin evolution and sediment provenance and place the basin-scale record within a regional context to illuminate the lithospheric processes driving extension and subsidence. The Muddy Creek Basin is an extensional half graben in southwest Montana that is \sim 22 km long and \sim 7 km wide, with a >800-m-thick sedimentary package. Basin deposition began ca. 49 Ma, as marked by multiple ignimbrites sourced from the Challis volcanic field, which are overlain by a tuffaceous fluvial section. Fluvial strata are capped by a 46.8 Ma Challis ignimbrite constrained by sanidine 40Ar/39Ar dating. An overlying fossiliferous limestone records the first instance of basinal ponding, which was coeval with the cessation of delivery of Challis volcanics-derived sediment into the Green River Basin. We attribute initial ponding to regional drainage reorganization and damning of the paleo-Idaho

H.E. Thoresen https://orcid.org/0009-0006 -6647-1130 †haleyt@uidaho.edu

GSA Bulletin; published online 13 February 2024

Basin and backfilling of the Lemhi Pass paleovalley. Detrital zircon maximum depositional ages and sanidine 40Ar/39Ar ages show alternating fluvial sandstone and lacustrine mudstone deposition from 46 Ma to 40 Ma in the Muddy Creek Basin. Sediment provenance was dominated by regionally sourced, Challis volcanics-aged and Idaho Batholithaged grains, while detrital zircon (U-Th)/He (ZHe) data are dominated by Eocene cooling ages. Basin deposition became fully lacustrine by ca. 40 Ma, based on an increasing frequency of organic-rich mudstone with rare interbedded sandstone. Coarse-grained lithofacies became prominent again starting ca. 37 Ma, coeval with a major shift in sediment provenance due to extension and local footwall unroofing. Detrital zircon U-Pb and corresponding ZHe ages from the upper part of the section are predominantly Paleozoic in age, sourced from the Paleozoic sedimentary strata exposed in the eastern footwall of the Muddy Creek detachment fault. Paleocurrents shift from south- to west-directed trends, supporting the shift to local sources, consistent with initiation of the Muddy Creek detachment fault. Detrital zircon maximum depositional ages from the youngest strata in the basin suggest deposition continuing until at least 36 Ma. These data show that extension in the Muddy Creek Basin, which we attribute to continued lithospheric thermal weakening, initiated \sim 10 m.y. later than in the Anaconda and Bitterroot metamorphic core complexes. This points to potentially different drivers of extension in western Montana and fits previously proposed models of a regional southward sweep of extension related to Farallon

INTRODUCTION

Extension is a fundamental tectonic process responsible for the collapse of orogenic belts, and a deeper understanding of extensional processes provides insights into the mantle and slab dynamics controlling the transition from contractional to extensional deformation. Mesozoic-Paleocene retro-arc contractile deformation and its sedimentary and structural record in the western United States are well preserved and have been extensively studied (e.g., DeCelles, 1994, 2004; Currie, 2002; Fuentes et al., 2011; Yonkee and Weil, 2015; Carrapa et al., 2019; Pujols and Stockli, 2021). However, multiple episodes of overprinting extension and voluminous felsic magmatism have made the timing and drivers of orogenic demise difficult to decipher (e.g., Coney and Harms, 1984; Livaccari, 1991; M'Gonigle and Dalrymple, 1996; Constenius, 1996; Chetel et al., 2011; Schwartz and Schwartz, 2013). Extension in Cordilleran-style orogens is accommodated in multiple ways with varying magnitudes, including emplacement of dikes (e.g., Simonsen, 1997; Gaschnig et al., 2010), detachment faults associated with metamorphic core complexes with >10 km of displacement (e.g., Coney and Harms, 1984; Foster and Asaf, 2002; O'Neill et al., 2004; Foster et al., 2010), low-angle detachment faults associated with <10 km of displacement (e.g., Constenius, 1996; Janecke et al., 1999; Janecke, 2007), and high-angle normal faults associated with Basin and Range-style extension and highly variable amounts of displacement (1-20 km; e.g., Stockli et al., 2002; Janecke and Blankenau, 2003; Parsons, 2006; Colgan et al., 2006) (Fig. 1). Multiple drivers have been invoked to explain western US Cordilleran extension, including gravitational collapse of thickened crust (e.g., Coney and Harms, 1984; Coney, 1987; Constenius, 1996; Fuentes et al., 2011)

https://doi.org/10.1130/B37268.1.

slab removal.

For permission to copy, contact editing@geosociety.org © 2024 Geological Society of America

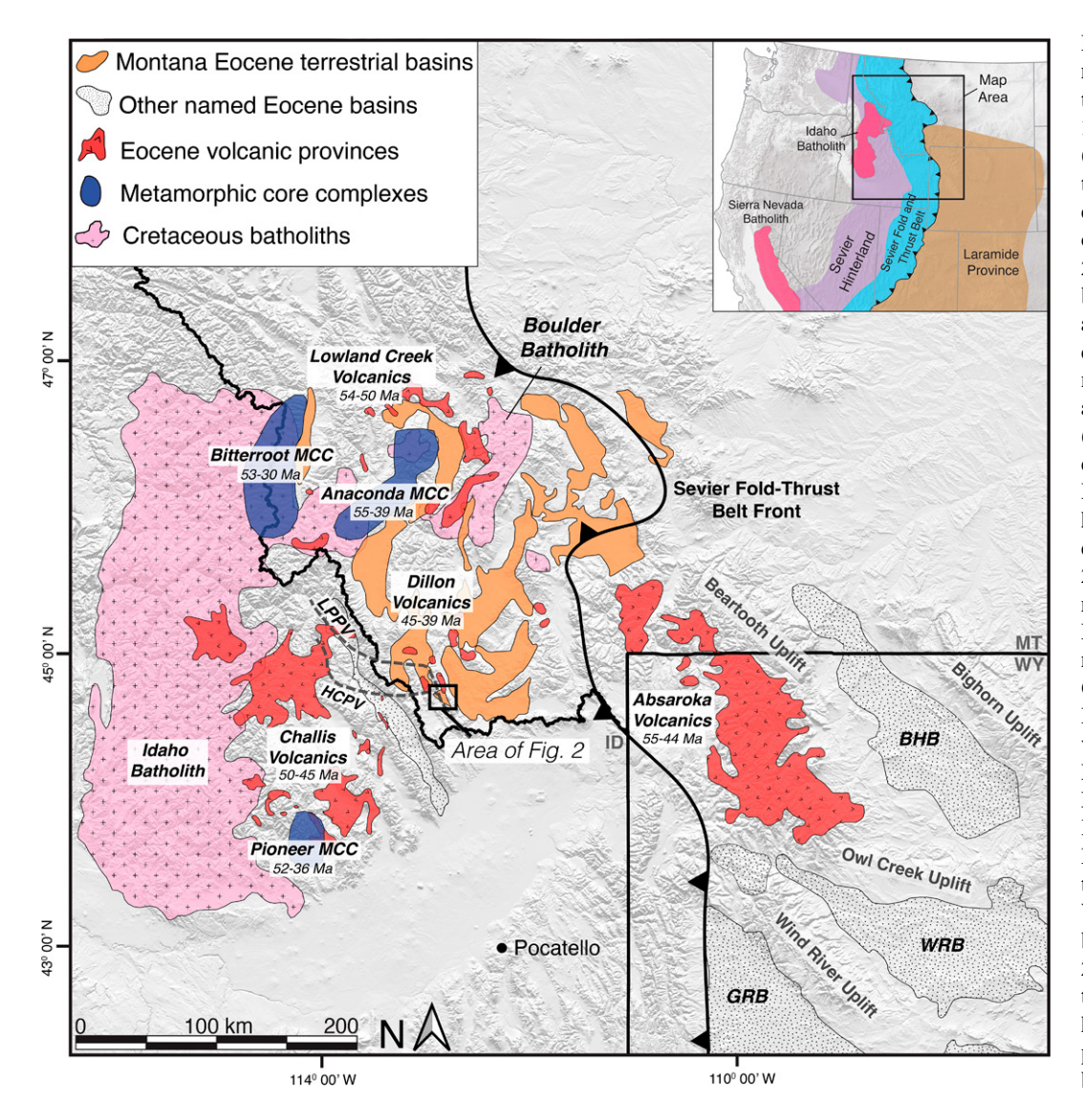


Figure 1. Simplified geologic map of study area with Eocene terrestrial basins (Constenius, 1996), volcanic provinces (Scarberry et al., 2021), Cretaceous batholiths (Scarberry et al., 2021), metamorphic core complexes (Whitney et al., 2013), and Wyoming lacustrine basins (Smith et al., 2008). Metamorphic core complex (MCC) exhumation ages and volcanic province crystallization ages are shown below labels (Foster and Asaf, 2002; Foster et al., 2010; Chetel et al., 2011; Howlett et al., 2021). Paleovalley tracts are shown by gray, dashed lines (Janecke et al., 2000). AC-Anaconda metamorphic core complex; BHB-Bighorn Basin; BR-Bitterroot metamorphic core complex; GRB—Green River Basin; HCPV-Hawley Creek paleovalley; ID-Idaho; LPPV-**Pass** Lemhi paleovalley; MT-Montana; WRB-Wind River Basin; WY-Wyoming. Inset: Map of western US tectonic provinces (Yonkee and Weil, 2015) and Cretaceous batholiths (Whitney et al., 2013). Blue-Sevier fold-andthrust belt; purple—Sevier hinterland; brown-Laramide province; pink—Cretaceous batholiths.

due to changing plate-boundary conditions (e.g., Liu and Shen, 1998; Henry, 2008), thermal weakening of the lithosphere through shallow slab removal (e.g., Sonder and Jones, 1999; Bendick and Baldwin, 2009; Hyndman, 2017) and/or delamination (e.g., Humphreys, 1995; Cassel et al., 2018), and reactivated motion on thrust faults or other preexisting weaknesses in the crust (e.g., Janecke, 2007; Druschke et al., 2011; Schwartz et al., 2019). There are stark differences in the magnitude and distribution of extension locally throughout the northern Basin and Range in Montana and Idaho, signifying potential differences in driving mechanisms (Fig. 1). Key questions about the large-scale crustal and lithospheric processes controlling extension and late orogenic to postorogenic evolution can be answered through the study of basinal stratigraphic records, which record initial crustal thickness, timing of deformation,

sediment provenance and routing, and associated changes in plate-boundary conditions.

The Muddy Creek Basin is an extensional half graben in southwest Montana (Fig. 2), a region that has undergone extensional deformation since the early Eocene (Fig. 3; Dunlap, 1982; Constenius, 1996; Janecke et al., 1999; Schwartz et al., 2019). It is one of the few basins in the northern Rocky Mountains with no documented Neogene sedimentary record preserved (Schwartz et al., 2019; Vuke, 2020), indicative of limited post-Oligocene extension and basin subsidence. Later extensional deformation has resulted in significant basin inversion and exposure of the Eocene sedimentary strata, recording both the initiation of subsidence and the long-term basin evolution, a rarity for the region (Janecke et al., 1999). In this study, we applied zircon U-Pb and (U-Th)/He double dating and sanidine 40Ar/39Ar dating to decimeter-scale measured stratigraphic sections of fluvial and lacustrine strata (Fig. 2) to improve depositional age control, track sediment provenance, and reconstruct a detailed model for basin and landscape evolution across the early Cenozoic. This basin evolution model allows us to further understand the larger lithospheric and mantle processes controlling the timing and magnitude of extensional deformation related to orogenic demise in the North American Cordillera.

BACKGROUND

Shallowing of Farallon plate subduction during the Late Cretaceous (e.g., Humphreys, 2009) shifted the orientation of contraction to southwest-northeast and initiated thick-skinned, Laramide-style thrusting as early as 100 Ma in Montana and lasting until 40 Ma (Fig. 3; Humphreys, 2009; Carrapa et al., 2019). Although

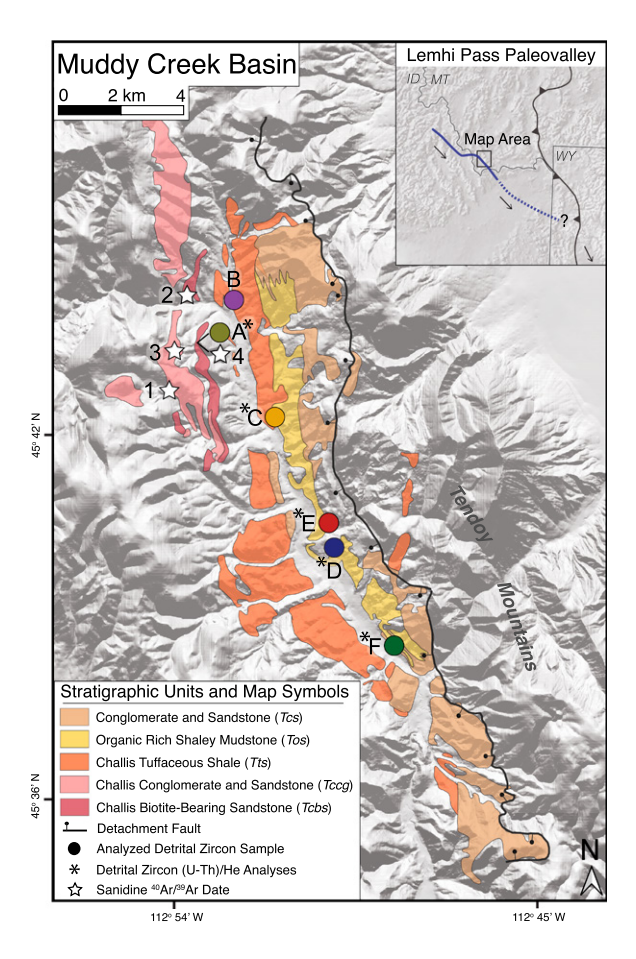


Figure 2. Simplified geologic map of the Muddy Creek Basin with detrital zircon and sanidine sample locations noted. Mapped stratigraphic units and detachment fault locations are from Lonn et al. (2003). Inset: Location of proposed Lemhi Pass paleovalley (blue line) in relation to the study area (Janecke et al., 2000). Black arrows denote paleoflow direction (Janecke et al., 2000; Schwartz and Graham, 2017). ID—Idaho; MT-Montana; WY—Wyoming.

eastward migration of Sierran arc volcanism ceased, magmatism continued to the north in the Idaho Batholith and other associated magmatic centers until ca. 45 Ma (Figs. 1 and 3; e.g., Gaschnig et al., 2010; Scarberry et al., 2021). Following Laramide shortening and crustal thickening in the Sevier foreland, progressive removal of the Farallon shallow slab via slab rollback and delamination produced voluminous volcanism in the Challis, Lowland Creek, Dillion, and Absaroka volcanic fields starting ca. 53 Ma and continuing into the middle Eocene, when volcanism migrated farther southwestward (Figs. 1 and 3; e.g., Moye, 1988; Humphreys, 1995, 2009; Dickinson, 2004; Henry, 2008; Dudás et al., 2010; Chetel et al., 2011; Cassel et al., 2018; Porter et al., 2019). Thermal and isostatic adjustments to new heat and magmatism in response to the removal of the Farallon slab also led to subsidence and initiation of basin deposition. In the central Rocky Mountains, slab dynamics have been constrained by the surface record of basin accumulation, paleoelevation studies, and detrital thermochronology (Smith et al., 2014; Cassel et al., 2018; Canada et al., 2020), but the surface record for the northern Rocky Mountains is less well developed. Moreover, it is not entirely clear whether the Farallon slab was one continuous curtain (Dickinson, 2004; Liu and Stegman, 2011; Smith et al., 2014) or multiple slabs delin-

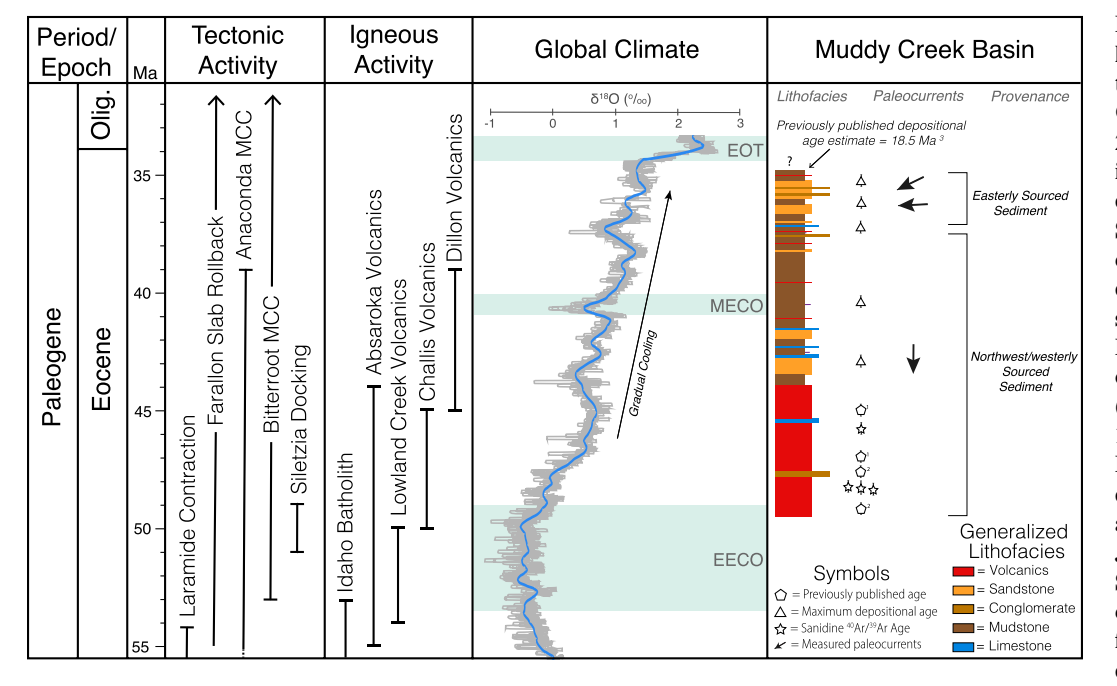


Figure 3. Comparative time line showing western Montana tectonic activity (De-Celles, 2004; Foster et al., 2010; Schwartz et al., 2019), igneous activity (Gaschnig et al., 2010; Chetel et al., 2011; Scarberry et al., 2021), global climatic trends (Westerhold et al., 2020), and a generalized stratigraphic column in the Muddy Creek Basin with depositional ages and provenance (M'Gonigle and Dalrymple, 1996; Janecke et al., 1999). Muddy Creek Basin references include: 1-M'Gonigle and Dalrymple (1996); 2— Janecke et al. (1999); 3-Schwartz et al. (2019). Global climatic records use benthic foraminifera (Westerhold et al., 2020). Grav line repre-

sents smoothed locally weighted function over 20 k.y.; blue line represents smoothed locally weighted function over 1 m.y. Green boxes highlight climatic events. ⁴⁰Ar/³⁹Ar ages are shown relative to 28.201 Ma calibration of Kuiper et al. (2008). Olig.—Oligocene; MCC—metamorphic core complex; EOT—Eocene–Oligocene transition; MECO—middle Eocene climatic optimum; EECO—early Eocene climatic optimum.

eated by tears (Humphreys, 1995, 2009). The early Eocene timing of Siletzia terrane accretion further adds to the uncertainty (Fig. 3; Schmandt and Humphreys, 2011; Wells et al., 2014). Additionally, basement thermochronology and sedimentary basin analysis of the hinterland belt of metamorphic core complexes show that extensional collapse often accompanies volcanism during slab rollback (e.g., Coney and Harms, 1984; Constenius, 1996; Foster and Asaf, 2002; Foster et al., 2010; Whitney et al., 2013; Canada et al., 2020).

In southwest Montana, Sevier- and Laramidetype thrust faults and folds were subsequently overprinted by two Cenozoic metamorphic core complexes, voluminous silicic magmatism, multiple extensional faults with varying amounts of displacement, and associated sedimentary basins (Fig. 1). Basement thermochronometry suggests that initiation of exhumation began no later than ca. 56-52 Ma in both the Bitterroot and Anaconda metamorphic core complexes (Fig. 3; House et al., 2002; O'Neill et al., 2004; Foster et al., 2010). Janecke et al. (1999) assigned younger ages (50-23 Ma) to continued lowermagnitude detachment faulting across western Montana, which they hypothesized occurred along structural culminations within the Sevier fold-and-thrust belt. The Muddy Creek supradetachment basin is one of several potential collapsed culminations that preserve an extensive Paleogene sedimentary record in response to <5 km of extension (Fig. 2; Janecke et al., 1999, 2000; Janecke, 2007).

Deposition of the Renova Formation

Cenozoic sedimentary rocks within the Muddy Creek Basin have been correlated to the Renova Formation, originally described by Kuenzi and Fields (1971; see also Dunlap, 1982; Janecke et al., 1999; Rothfuss et al., 2012; Schwartz and Schwartz, 2013; Schwartz et al., 2019). Early studies suggested that the Renova Formation filled multiple individual basins separated by paleohighs, based on stratigraphy and conglomerate clast provenance, similar in configuration to modern geography (Fig. 1; Pardee, 1950; Kuenzi and Fields, 1971; Hanneman, 1989). Later studies cited sedimentologic, provenance, and geochronology data to interpret that the Renova Formation blanketed a low-relief landscape in southwest Montana that was subsequently bifurcated by extension (Fritz and Sears, 1993; Fritz et al., 2007). The Renova Basin has also been interpreted to lie along the eastern edge of a north/northwest-trending Oligocene rift corridor and to represent a single connected basin called the Renova Basin (Janecke, 1994; Janecke and Blankenau, 2003). Other recent studies, however,

interpreted that the Renova Formation was deposited in individual basins by through-going fluvial systems (Fig. 1; Janecke et al., 1999; Rothfuss et al., 2012; Schwartz and Schwartz, 2013).

Early work subdivided the Renova Formation based on lithologic variability and North American Land Mammal Age (NALMA) fossil assemblages (Dunlap, 1982; Fields et al., 1985; Hanneman and Wideman, 1991), with more recent 40Ar/39Ar dating of volcanic ashes and detrital zircon maximum depositional ages (MDAs) corroborating NALMA ages and indicating that Renova Formation deposition occurred regionally from ca. 43 Ma to 19 Ma (Janecke and Snee, 1993; M'Gonigle and Dalrymple, 1996; Link et al., 2008; Schwartz and Graham, 2017), with individual basins having different depositional periods (Constenius, 1996; Schwartz et al., 2019). Renova Formation lithology varies substantially within each basin: Basin-margin alluvial facies commonly interfinger with interior fluvial and lacustrine facies, and there are well-developed paleosol horizons, volcanic ash beds, and numerous intrabasinal unconformities (Hanneman and Wideman, 1991; Schwartz and Schwartz, 2013). This variability, along with disparate depositional age control, make interbasin correlations across southwest Montana difficult, resulting in differential divisions of members of the Renova Formation between different basins (Hanneman and Wideman, 1991; Fritz et al., 2007; Schwartz and Schwartz, 2013; Schwartz and Graham, 2017; Schwartz et al., 2019). Regionally, the Renova Formation is overlain unconformably by the Miocene Six Mile Creek Formation in multiple western Montana basins (Kuenzi and Fields, 1971; Schwartz and Schwartz, 2013).

Muddy Creek Basin

Dunlap (1982) documented five lithofacies in the Renova Formation of the Muddy Creek Basin: coarse tuffaceous sandstone, fine tuffaceous sandstone, shale/sandstone, sandstone/ conglomerate, and volcanic rock (Fig. 2). Depositional environments were interpreted to have been predominantly lacustrine with interfingering fan-delta and alluvial-fan deposits (Dunlap, 1982). Plant fossils, ostracods, pelecypods, and freshwater gastropods were used to assign a late Eocene to Oligocene depositional age to the lacustrine strata (Dunlap, 1982). These ages do not precisely constrain the upper part of the section due to large uncertainties on faunal ages, where estimates range from late Eocene to early Miocene (Fig. 3; Dunlap, 1982; Janecke et al., 1999).

Janecke et al. (1999) conducted mapping at 1:24,000 scale and ⁴⁰Ar/³⁹Ar geochronology

to conclude that initial slip along the basinbounding normal faults occurred during the final phases of Challis volcanism. Conglomerate clast counts and lithofacies analysis showed that sediment was deposited in a series of coalescing alluvial fans locally sourced from both the hanging wall and footwall of the Muddy Creek detachment fault (Fig. 2; Janecke et al., 1999). Based on the age of two Challis ignimbrites near the base of the section dated at 47.07 ± 0.16 Ma and 49.47 ± 0.05 Ma, they concluded that the Muddy Creek Basin began filling ca. 49 Ma, and deposition continued into the Oligocene (M'Gonigle and Dalrymple, 1996; Janecke et al., 1999). Janecke et al. (2000) proposed that the Muddy Creek Basin was once part of the Cretaceous Lemhi Pass paleovalley that flowed from the Salmon River Mountains to northwest Wyoming (Fig. 2, inset), based on the provenance of quartzite clasts in the Harebell and Pinyon conglomerates located in southeast Idaho and western Wyoming (Kraus, 1985; Janecke et al., 2000). This was supported by 40Ar/39Ar dating of Challis-derived detrital feldspar grains found in the Green River Basin dated between 50 Ma and 47.5 Ma (Chetel et al., 2011). The Lemhi Pass paleovalley eventually filled with Challis volcanics, but previous studies have not constrained the driving mechanism behind basin subsidence that provided accommodation for the accumulation of ~830 m of lacustrine and fluvial rocks that constitute the basin fill of Muddy Creek Basin (Janecke et al., 1999, 2000).

Isotopic studies have also been conducted in the upper lacustrine facies of the basin using stable isotope ratios (δ^{18} O and δ^{13} C) of pedogenic carbonate nodules (Methner, 2016; Schwartz et al., 2019). The δ^{18} O values range from 15% to 19%, and δ^{13} C values range from -7% to -3%o. These data points were assigned a late Eocene to Oligocene age based on previous faunal age controls, which had an age range of late Eocene to late Oligocene, making it difficult to compare this dataset to global climatic trends (Dunlap, 1982; Methner, 2016). Both studies proposed a period of significant aridification during the late Eocene. They concluded that the conditions controlling $\delta^{18}O$ and $\delta^{13}C$ values were local, with variability related to the development of growing topography. Atmospheric circulation, temperature, and precipitation had more control on δ^{18} O and δ^{13} C values over time than did interbasin conditions (Methner, 2016; Schwartz et al., 2019).

METHODS

Stratigraphic sections were measured in the Muddy Creek Basin at decimeter scale to record fine-scale changes in lithofacies and sediment

TABLE 1. MAXIMUM DEPOSITIONAL AGE AND MAXIMUM LIKELIHOOD AGE CALCULATIONS WITHIN THE MUDDY CREEK BASIN, WITH SAMPLES LISTED IN STRATIGRAPHIC ORDER

Sample name	Map name*	YSG [†] (Ma)	Youngest clu 2+ overlappi within 1σ e	ng ages	Youngest cluster of 3+ overlapping ages within 2σ error†		MLA [§] (Ma)	Preferred MDA (Ma)		Sample location (WGS84)	
			YC1σ(2+) (Ma)	No. of grains	YC2σ(3+) (Ma)	No. of grains			Latitude (°N)	Longitude (°W)	
MT21-553MC	F	36.0 ± 0.64	50.9 ± 0.78	2	432.6 ± 1.7	8	326.5 ± 7.29	36.0 ± 0.64	44.64241	112.81036	
MT21-541MC	E	$\textbf{36.8} \pm \textbf{1.9}$	$\textbf{412.8} \pm \textbf{2.98}$	3	$\textbf{412.8} \pm \textbf{2.98}$	3	246.77 ± 3.58	$\textbf{36.8} \pm \textbf{1.9}$	44.67643	112.83697	
MT21-539MC	D	36.5 ± 1.4	37.0 ± 0.46	3	37.1 ± 0.42	3	259.2 ± 13.7	37.1 ± 0.42	44.66959	112.83479	
MT20-474MC	С	37.0 ± 0.88	40.2 ± 0.64	3	40.4 ± 0.48	3	37.14 ± 1.84	40.4 ± 0.48	44.70568	112.85835	
MT21-549MC	В	42.8 ± 0.76	$\textbf{45.2} \pm \textbf{0.52}$	3	$\textbf{45.3} \pm \textbf{0.56}$	4	43.01 ± 0.97	43.01 ± 0.97	44.73746	112.8745	
MT20-468MC	Α	41.2 \pm 1.1 Ma	44.5 ± 0.36	4	44.3 ± 0.32	5	41.99 ± 1.24	44.32 ± 0.32	44.72575	112.88901	

Note: YSG—youngest single grain; MLA—maximum likelihood age; MDA—maximum depositional age; WGS84—World Geodetic System 1984. Calculated uncertainties are reported at the 2σ level. See Figures S1 and S2 (text footnote 1) for MDA calculations.

provenance, and to provide a detailed record of sampling locations within the stratigraphy. Covered or weathered exposures were trenched to facilitate measurement of fresh, complete sections when possible. Lithofacies were assigned throughout the basin based on bed geometry, grain-size trends, biogenic features (e.g., leaf fossils and gastropods), and sedimentary structures, and they are described in the results below. Complete detailed stratigraphic sections and sedimentologic data can be found in the Supplemental Material¹ (Figs. S4-S12; Table S5). Sandstone, conglomerate (both matrix and clasts), and volcanic ash (ignimbrites and ash-fall tuffs) were sampled from within the stratigraphic sections for geochronologic and thermochronologic analyses. A wide range of grain sizes was sampled to prevent any grainsize biases and capture the provenance within a range of depositional environments, although previous work has shown that grain size exerts limited control on the U-Pb age spectra produced (Leary et al., 2020). The new measured sections are the basis for depositional environment interpretations, and coupled with new geochronology and thermochronology, they provide a record of basin evolution and its relationship to regional extension.

Detrital Zircon U-Pb and (U-Th)/He Double Dating

Six samples of sandstone and conglomerate were collected from the Muddy Creek Basin for detrital zircon U-Pb and (U-Th)/He double

dating to elucidate sediment provenance, depositional age, and exhumation age (Table 1). Zircon grains were separated using conventional separation techniques including crushing, Gemini table, heavy liquid, and magnetic separation procedures in the Tectonics and Basin Analysis Laboratory at the University of Idaho. Final separates were mounted on double-sided tape on a 2.5 cm acrylic disk. Detrital zircon U-Pb geochronology was carried out at the UTChron Laboratory at the University of Texas, Austin, via depth-profile high-resolution laser ablationinductively coupled plasma-mass spectrometry (LA-ICP-MS) following the procedures of Pujols and Stockli (2021). The primary standard used was GJ1 (608.5 \pm 0.37 Ma; Jackson et al., 2004); Plešovice (337.13 \pm 0.37 Ma; Slama et al., 2008) was used as a secondary standard. Iolite3.7 (Paton et al., 2011) and VizualAge (Petrus and Kamber, 2012) were used to perform age calculations from baseline-corrected intensities. No correction was made for common Pb, but common Pb was graphically evaluated, and analyses were rejected when high-common-Pb zones were present. Zones within the zircon grain were excluded based on elevated ²⁰⁶Pb/²⁰⁷Pb ratios relative to the concordant part of the grain, and zones were selected where the age was constant and not affected by high ²⁰⁶Pb/²⁰⁷Pb values. Isotopic ages and ratio errors are reported as 2σ absolute errors. For detrital zircon age spectra interpretations, the ²⁰⁷Pb/²⁰⁶Pb age is reported for grains older than 850 Ma, and the ²⁰⁶Pb/²³⁸U age is reported for grains younger than 850 Ma. The 850 Ma cutoff was chosen due to the presence of grain age populations between 1000 Ma and 900 Ma to ensure that all grains in this population were calculated using the same isotopic ratios, keeping the interpretation of these ages consistent. Ages that were >30%discordant were excluded from interpretations. Full analytical methods and results are reported in Supplemental Text S1 and Table S1.

Following detrital zircon U-Pb analysis, a subset of zircon grains from five samples was selected for (U-Th)/He analyses, which were performed at the UTChron Laboratory at the University of Texas at Austin (two samples) or Basin Analysis & Helium Thermochronology Laboratory (BAHTL) at the University of Connecticut (three samples), with methods described separately below. Zircon grains were chosen with a wide range of U-Pb crystallization ages, with the exception of ages associated with Eocene volcanism (younger than 55 Ma). Crystals were then handpicked and screened for quality, crystal size, shape, and inclusions in the Tectonics, Topography, Thermochronology (T₃) laboratory at the University of Idaho. Measurements were made to calculate crystal mass and alpha-ejection correction factors following Ketcham et al. (2011) and Cooperdock et al. (2019). Individual crystals were placed into 1 mm Nb packets. At BAHTL, packets were placed under an ultrahigh vacuum ($\sim 5 \times 10^{-9}$ torr) and heated to 1200 °C for 15 min to extract radiogenic 4He. Cryogenically purified and gettered ⁴He was spiked and analyzed on a quadrupole mass spectrometer. This extraction process was repeated until ⁴He yield was <2% of initially extracted gas. Degassed grains were sent to the Thermochronology Research and Instrumentation Laboratory (TRaIL) at the University of Colorado, Boulder, for U and Th measurements. Individual grains within the Nb packets were spiked and dissolved (including the Nb packet) via Parr digestion vessels in HF, HNO₃, and HCl and then diluted with doubly deionized water. Solutions were analyzed using a Thermo Element 2 magnetic sector mass spectrometer for U and Th contents. These measurements were combined with measured He and grain data to calculate He dates, which are reported at $\pm 1\sigma$ uncertainty following alpha-ejection (F_T) correction. Full analytical methods are reported in Supplemental Text S1.

^{*}See Figure 2.

[†]Dickinson and Gehrels (2009).

[§]Vermeesch (2021).

¹Supplemental Material. Zircon (U-Pb), zircon (U-Th)/He, and sanidine ⁴⁰Ar/³⁰Ar datasets, as well as full stratigraphic sections and maximum depositional age calculations. Please visit https://doi.org/10.1130/GSAB.S.24944781 to access the supplemental material, and contact editing@geosociety.org with any questions.

For aliquots run in the UTChron Laboratory, zircons picked had a minimum width of 70 µm with euhedral grain morphology and were measured and then packed in acid-cleaned Pt tubes. Each grain was heated with a diode laser at ~1300 °C for 10 min to extract ⁴He and then was reheated for an additional 10 min at 1300 °C until ⁴He yield reached <1%. Following degassing, grains were unpacked from the Pt packets and dissolved using a two-step hydrofluoricnitric acid and hydrochloric acid pressure vessel digestion over a period of 4 days. Solutions were spiked and analyzed for their U, Th, and Sm concentrations using a Thermo Element 2 ICP-MS. Alpha-ejection corrections (F_T) were calculated using the Helios software, and ages are reported with standard error (\sim 8%) based on the reproducibility of the Fish Canyon Tuff standard (Reiners et al., 2002; Hart et al., 2017). Full analytical procedures are described in Wolfe and Stockli (2010).

Radiation damage in zircon crystals can lead to anomalous zircon He ages (Guenther et al., 2013; Ketcham et al., 2013). This becomes of greater concern for grains with pre-Cenozoic cooling histories; to reduce this effect, we selected grains that had eU concentrations <900 ppm based on the LA-ICP-MS detrital zircon U-Pb analyses of the same grains, and we avoided any metamict grains (Ault et al., 2019). Following (U-Th)/He analyses, effects from radiation damage were checked by plotting the F_T-corrected He age versus eU, and no correlation was found in any of the samples.

Detrital Zircon Maximum Depositional Ages

The youngest zircon crystallization ages from within a detrital zircon age population can be used to calculate a detrital zircon MDA, which is based upon the assumption that the host rock cannot be older than the youngest crystallization age, but it also cannot be younger than the present (Dickinson and Gehrels, 2009). For the purposes of the Muddy Creek Basin, we interpreted our calculated MDAs to closely represent the true depositional age due to voluminous coeval

volcanism in southwest Montana and surrounding regions, and an upward younging of MDAs at a reasonable geologic rate (Figs. 1 and 3; Chetel et al., 2011). Multiple statistical methods for calculating MDAs have been outlined in Dickinson and Gehrels (2009) and Vermeesch (2021). We calculated and compared the four following methods: (1) crystallization age of the youngest single grain (YSG), (2) the youngest cluster of two or more overlapping ages within 1σ error (YC1 σ [2+]), (3) the youngest cluster of three or more overlapping ages within 2σ error (YC2σ[3+]), and (4) maximum likelihood age (MLA) (Dickinson and Gehrels, 2009; Vermeesch, 2021). We used $YC2\sigma(3+)$ and MLA for primary interpretation of most samples because these are the most conservative methods, except for samples MT21-541MC and MT21-553MC, where we used YSG due to the lack of other grains within overlapping uncertainty (Table 1). While this metric is less statistically robust, we believe it is likely near true depositional age or slightly older due to agreement with $YC2\sigma(3+)$ ages and 40Ar/39Ar ages (Tables 1 and 2), the presence of volcanic grains throughout the section, and known volcanic sources of similar age (Fig. 3).

Sanidine 40Ar/39Ar Geochronology

Four felsic ignimbrites and air-fall tuffs were sampled from locations within the Muddy Creek Basin for sanidine ⁴⁰Ar/³⁹Ar dating (Fig. 2). Sanidine phenocrysts were separated via crushing, sieving, leaching in dilute HCl and HF, and handpicking under refractive index oils. Sanidine crystals were irradiated at the Oregon State University TRIGA reactor in the Cadmium-Lined In-Core Irradiation Tube (CLICIT) using the 28.201 Ma Fish Canyon sanidine standard (Kuiper et al., 2008). A 55 W CO2 laser located in the WiscAr laboratory (University of Wisconsin-Madison) was used to perform single-crystal fusion experiments. Gas analysis was conducted on a Nu Instruments Noblesse multicollector mass spectrometer as outlined in Jicha et al. (2016). Argon beam intensities were corrected for baselines, blanks, radioactive decay, and detector intercalibration, the latter of which was done using an in-house cocktail gas (Jicha et al., 2016). Weighted mean ages were calculated using the decay constants of Min et al. (2000) and are reported with analytical uncertainties at the 95% confidence level including the J uncertainty. All analytical results are reported in Table 2 and Table S2.

RESULTS

General Stratigraphy of the Muddy Creek Basin

The Muddy Creek Basin consists of a basal package of volcanic and volcaniclastic strata overlain by a package of mudstone with interbedded sandstone and conglomerate with limited interbedded volcaniclastic material (Fig. 4A). The base of the section consists of a 5.4-m-thick ignimbrite dated in this study using sanidine 40 Ar/ 39 Ar at 48.24 \pm 0.07 Ma (Table 2). This is overlain by 42 m of poorly exposed volcaniclastic and volcanic material, based on soil color and float composition, and a 34-m-thick section of interbedded volcaniclastic sandstone and conglomerate. This section includes at least three additional biotite-rich ignimbrites that are laterally continuous over 10-40 m and range in thickness from 0.3 m to 5.6 m (Fig. 4B). Based on the range of ages and regional correlations between deposits, this volcanic material was sourced from the Challis volcanic field in what is now Idaho (Fig. 1; M'Gonigle and Dalrymple, 1996; Janecke et al., 1999, 2000). The basal volcanic and volcaniclastic section is overlain by a 743-m-thick succession of mudstone interbedded with conglomerate, sandstone, and bentonite. Our detailed stratigraphic analysis provided decimeter-scale resolution of lithologic variations in basin strata not documented in previous 1:24,000 scale mapping (Fig. 2; based on Dunlap, 1982; Lonn et al., 2003). We describe the basin fill in the context of 19 measured sections, constituting descriptions for a total of 830 m of section, and we differentiated 10 distinct lithofacies. See Figures S4-S12 for full stratigraphic sections.

TABLE 2. SUMMARY OF SINGLE-CRYSTAL 40 Ar/ 39 Ar ANALYSES ON CHALLIS IGNIMBRITES IN THE MUDDY CREEK BASIN

Sample name	Map name*	Single sanidine analyses	Age (Ma)	2σ error	MSWD	Latitude (°N)	Longitude (°W)
MT21-544MC	4	27/35	46.797	0.049	1.361	44.725913	112.888950
MT20-465MC	3	27/31	48.147	0.048	1.225	44.724940	112.892320
WU14-048ML-B	2	25/27	48.243	0.074	1.326	44.7369	112.894883
MT20-464MC	1	24/31	48.401	0.048	1.284	44.714480	112.910910

Note: Ages were calculated relative to the 28.201 Ma Fish Canyon sanidine (Kuiper et al., 2008), with interpreted weighted mean ages shown. Decay constants used were those of Min et al. (2000). Atmospheric $^{40}\text{Ar}/^{39}\text{Ar} = 298.56 \pm 0.62$ (Lee et al., 2006). For complete datasets, see Table S3 (text footnote 1). All sample locations use World Geodetic System 1984 (WGS84) projection. MSWD—mean squared weighted deviate. *See Figure 2.

Lithofacies Descriptions

Pebble-Cobble Conglomerate (G1)

Facies G1 consists of pebble- to cobblesized, imbricated, clast-supported conglomerate with subrounded to well-rounded clasts primarily composed of gray and brown quartzites, granodiorite, dark brown to tan siltstone, dark brown siltite, and tuff. Lenses of medium to very coarse sand are present within the conglomerate. Contacts are undulatory on the bottom, typi-

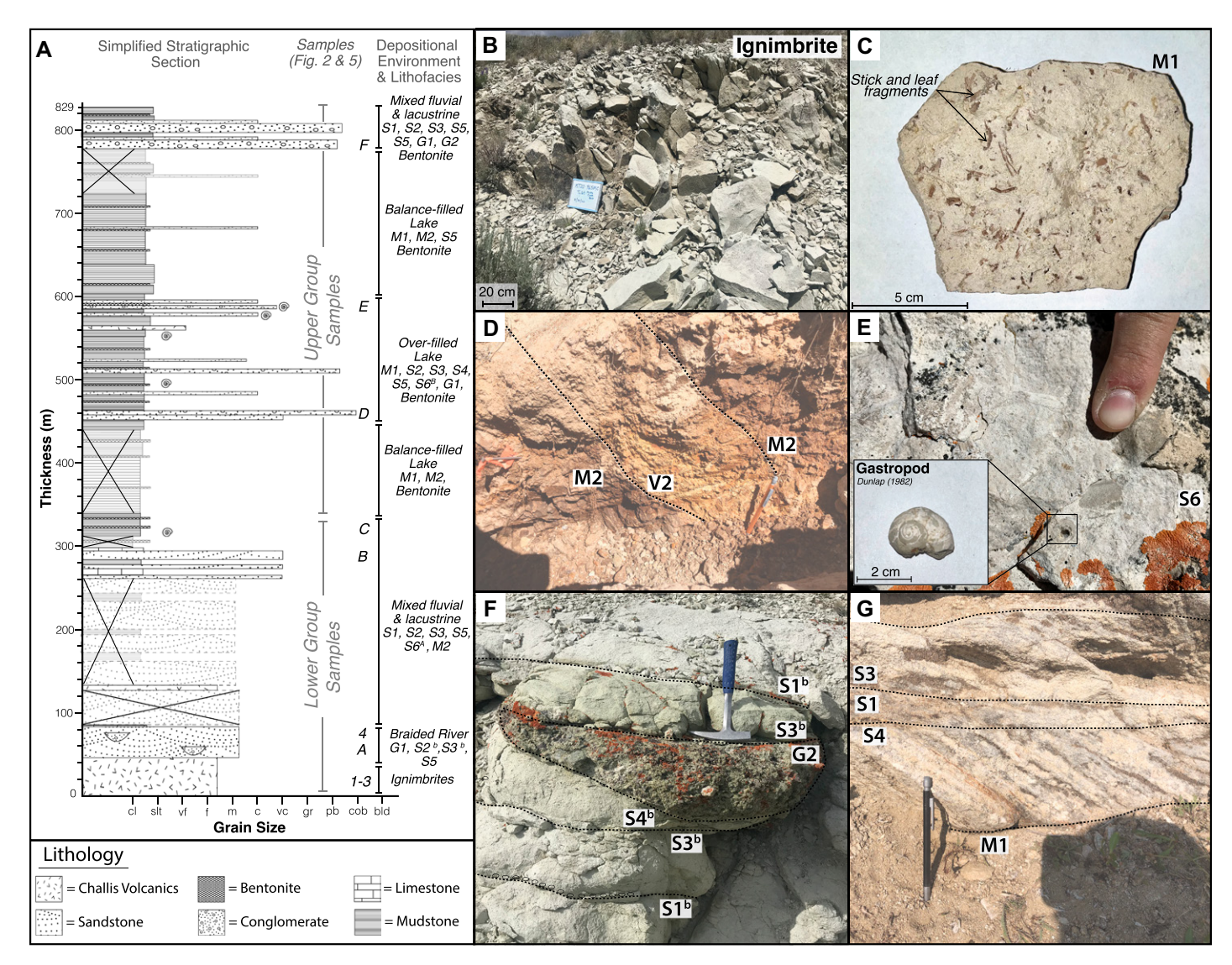


Figure 4. (A) Simplified stratigraphic section with interpreted depositional environments and lithofacies. Locations of samples within the stratigraphic section are shown, and labels correlate with Figure 2. Locations of known gastropod shells are shown. Sections with a black X indicate missing section. See Figures S4–S12 (text footnote 1) for full stratigraphic sections. Grain size abbreviations: cl—clay; slt—silt; vf—very fine; f—fine; m—medium; c—coarse; vc—very coarse; gr—granule; pb—pebble; cob—cobble; bld—boulder. (B) Challis ignimbrite in the basal portion of the basin. (C) Lithofacies M1. (D) Lithofacies M2 and V2. (E) Lithofacies S6 with an example of the gastropods found within the strata. (F) Volcaniclastic sandstones and conglomerates in the basal portion of the Muddy Creek Basin. (G) Cross-bedded sandstone capping organic-rich mudstone.

cally scoured into beds below, with flat upper contacts. Bed thickness ranges from 0.5 m to 5 m, possibly representing multiple amalgamated beds.

Granule-Pebble Conglomerate (G2)

Facies G2 consists of granule- to pebblesized, imbricated, clast-supported conglomerate with a medium- to coarse-grained sandy matrix (Fig. 4F). Clasts are well sorted and rounded. Facies G2^A clasts are primarily composed of gray and white quartzites and dark brown siltstone with rare tuff clasts. There are also oblong lenses of fine to coarse sand with dewatering structures. Facies G2^B has a volcaniclastic matrix with clasts primarily composed of pumice and rare purple quartzites. Contacts are undulatory with some outsized cobbles at the bottom of the bed. Bed thickness ranges from 0.2 m to 1.5 m.

Bioturbated Sandstone (S1)

Facies S1 consists of poorly sorted siltstone to subrounded, very coarse-grained sandstone with no visible internal structures. Outsized granule to pebble clasts and thin upward-fining successions are rarely present. Bioturbation and burrows are

common. Facies S1^A is primarily composed of detrital quartz and feldspar, with granule to pebble lags composed of gray and white quartzites, granodiorite, and dark brown siltite with occasional organic matter present (Fig. 4G). Facies S1^B is volcaniclastic and rich in detrital biotite with pebble lags primarily composed of pumice. Contacts are undulatory, and bed thicknesses range from 0.05 m to 0.6 m.

Planar Laminated Sandstone (S2)

Facies S2 consists of very fine- to coarsegrained, moderately sorted and rounded, planar laminated sandstone with occasional coarse-grained lags. Facies S2^A is tan/buff in color and is primarily composed of detrital quartz and feldspar grains. Facies S2^B is tuffaceous and rich in detrital biotite with granule to pebble lags composed of pumice clasts. Contacts are undulatory with upper contacts commonly scoured into by overlying coarser facies (G1, G2). Bedding thickness ranges from 0.04 m to 4 m.

Trough Cross-Stratified Sandstone (S3)

Facies S3 consists of very fine- to coarsegrained, poorly sorted, trough cross-stratified sandstone with pebble lags. Facies S3^A is primarily composed of detrital quartz and feldspar grains with <5% lithic grains (Fig. 4G). Facies S3^B is tuffaceous with pebble lags primarily composed of pumice (Fig. 4F). Detrital biotite grains are aligned along the foresets of the cross beds. Contacts are undulatory and are often scoured into by overlying, coarser beds. Bedding thickness ranges from 0.1 m to 1 m.

Planar-Tabular Cross-Stratified Sandstone (S4)

Facies S4 consists of fine- to coarse-grained, well-sorted, planar-tabular cross-stratified sand-stone. Grains have medium to high sphericity and medium roundness. Facies S4^A is primarily of composed of detrital quartz, feldspar, and clays (Fig. 4G). Facies S4^B is tuffaceous and rich in detrital biotite and has rare very coarse-grained to granule clasts of pumice. Contacts tend to be relatively flat on top and scoured on the bottom, especially when overlying a finer-grained bed. Bed thicknesses range from 0.05 m to 2.5 m.

Cross-Laminated Sandstone (S5)

Facies S5 consists of well-sorted and rounded, silt to medium-grained, cross-laminated sandstone. Pebble lags composed of gray quartzite, tuff, and dark brown silt are present. Detrital biotite grains occasionally align along the bottom of the foresets. Root casts may be present. Thin upward-fining successions rarely occur. Contacts are undulatory. Bed thicknesses range from 0.1 m to 0.3 m and vary laterally.

Fossiliferous Limestone (S6)

Facies S6^A consists of micritic, very finegrained limestone with gastropods (Fig. 4E), bivalves, algal mats, and other shelly debris. Facies S6^B consists of well-sorted packstone. Bed thicknesses range from 0.2 m to 0.8 m, with semi-wavy contacts and scours into finegrained beds below. Contacts are undulatory. Bedding thickness is variable, ranging from 0.2 m to 5 m.

Organic-Rich Mudstone (M1)

Facies M1 consists of organic-rich, dark red to brownish green mudstone with abundant sticks, leaves, gastropods, and bivalves (Fig. 4C). Silt to medium-grained oblong sand lenses with ripple laminations are present. Beds are laterally continuous and horizontally laminated at a millimeter scale, and bed thicknesses range from 0.2 m to 2 m.

Organic-Poor Mudstone (M2)

Facies M2 consists of organic-poor, laterally continuous, green to red, pedogenically altered silty claystone. Carbonate nodules and very coarse sand lenses are occasionally present. (Fig. 4D). Oxidation staining, burrowing, and color mottling are present in some beds. Contacts tend to be undulatory, and bed tops are commonly scoured. Bedding thicknesses range from 1 cm to 2 cm.

Detrital Zircon U-Pb Geochronology

Six detrital zircon samples yielded U-Pb dates ranging from Eocene to Archean. Samples MT20-468MC, MT21-549MC, and MT20-474MC (labeled A-C respectively in Fig. 2) are from the lower portion of the section (Fig. 4A). MT20-468MC (G2B) and MT20-474MC (S1) have grain age peaks at 49 Ma and 48 Ma, with subsidiary grain age peaks (n < 10) between 1700 Ma and 1400 Ma (Fig. 5A). MT21-549MC (S3^B) has a grain age peak at 70 Ma with subsidiary peaks between 1700 Ma and 1500 Ma (Fig. 5A). These three samples are distinct from samples in the upper part (Fig. 4A) of the section, MT21-539MC, MT21-541MC, and MT21-553MC (labeled D-F, respectively, in Fig. 2), which are dominated by Paleozoic and Precambrian grain ages with limited Cenozoic grain ages. MT21-539MC (G1), MT21-541MC (G2), and MT21-553MC (G1) (D-F in Fig. 5A) have age peaks at 432 Ma, 1160 Ma, 1500 Ma, 1630 Ma, 1720 Ma, and 1800 Ma, with subsidiary age peaks (n < 15) older than 2000 Ma and at 42 Ma, 45 Ma, and 46 Ma, respectively.

Detrital zircon MDAs were calculated from these U-Pb age distributions based on the methods described in Dickinson and Gehrels (2009) and Vermeesch (2021) and are summarized in Table 1. Lower group samples have calculated MDAs ranging from 44.3 ± 0.32 Ma to 40.4 ± 0.48 Ma. Upper group samples have calculated MDAs ranging from 37.1 ± 0.42 Ma to 36.0 ± 0.64 Ma (Table 1). Pb loss is a possibility with all calculated MDAs (Gehrels, 2014), and we identified one sample (MT20-468MC; Fig. 2, sample A) where it has affected the MDA based on disagreement with surrounding sanidine 40 Ar/ 39 Ar geochronology.

Sanidine 40Ar/39Ar Geochronology

We complemented calculated MDAs with four sanidine 40 Ar/ 39 Ar ages of interbedded ignimbrites, which was only possible in the lower part of the section (Fig. 2). Three ignimbrite samples from the lower portion of the stratigraphic section (Figs. 2 and 4A, samples 1–3) gave unimodal ages of 48.4 ± 0.05 Ma, 48.24 ± 0.07 Ma, and 48.15 ± 0.05 Ma with mean squared weighted deviate (MSWD) values of 1.28, 1.33, and 1.23 respectively. Sample MT21-544MC, located at the top of the basal fluvial stratigraphic section, gave a unimodal age of 46.8 ± 0.05 Ma with a MSWD value of 1.36. The number of single sanidine analyses used in each age calculation is shown in Table 2.

Detrital Zircon He Thermochronology

Twenty-four detrital zircon (U-Th)/He (ZHe) dates from grains with Eocene to Archean U-Pb crystallization ages from five of the detrital zircon samples in the Muddy Creek Basin ranged from 767 Ma to 41 Ma (Figs. 2 and 5B). Lower group samples MT20-468MC and MT20-474MC gave predominantly Eocene ZHe cooling ages, ranging from 54.7 Ma to 41.8 Ma, with one outlier Paleozoic ZHe cooling age of 399 Ma (Fig. 5B). Upper group samples MT21-559MC, MT21-541MC, and MT21-552MC gave predominantly Paleozoic ZHe cooling ages, ranging from 435 Ma to 261 Ma, with one Precambrian ZHe cooling age of 767 Ma (Fig. 5B).

INTERPRETATIONS

Lithofacies Interpretations

We investigated the frequency, distribution, and stacking patterns of lithofacies in tandem with new depositional age constraints to determine the depositional systems present in the Muddy Creek Basin and the timing of those depositional shifts. The basal tuffaceous (Fig. 4A, 30-80 m) fluvial package is laterally continuous, spanning over half the length of the ~30-km-long basin, and it was deposited between 48.5 Ma and 46 Ma (Fig. 2, map units Tcbs and Tccg). The presence of trough crossstratified sandstone beds (S3B) with upwardfining sequences, overlain by planar-tabular cross-stratified sandstone beds (S4B) and finergrained horizontally laminated sandstone (S2), represents deposition of aggrading channel-bar deposits fining upward into bar-top deposits, respectively (Walker and Cant, 1984). Coarsergrained, horizontally laminated sandstone (S2) overlying this upward-fining sequence is indicative of upper-stage flow deposition during times

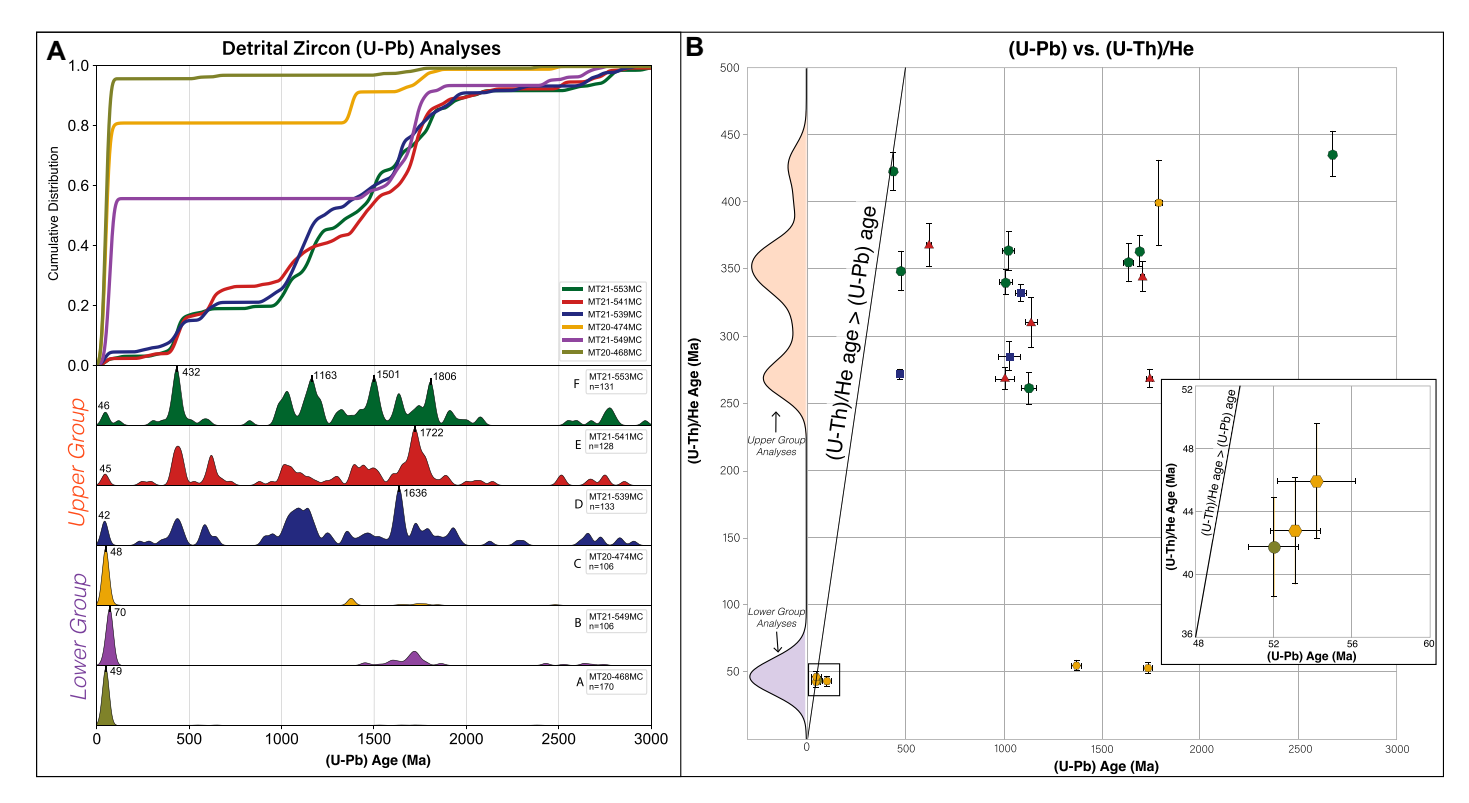


Figure 5. Summary figure of detrital zircon analyses in the Muddy Creek Basin. (A) Stacked kernel density estimates (KDEs) in stratigraphic order (where sample A = oldest), with labeled age peaks and a cumulative distribution function (CDF) summarizing all six samples. Number of grains analyzed per sample is listed below sample name. Kernel density estimate color correlates with sample colors in part B and sample location colors in Figure 2. KDEs and CDF were plotted using detritalPy (Sharman et al., 2018), with KDE bandwidth = 18. (B) Detrital zircon (U-Th)/He age (Ma) versus detrital zircon U-Pb age (Ma) with error bars representing 2σ error and a color-coded kernel density estimate on the y axis. Inset: U-Pb age (Ma) versus (U-Th)/He age (Ma) for the samples within the black box to show relation to 1:1 line.

of increased discharge (Cant and Walker, 1978; Skelly et al., 2003; Bridge and Lunt, 2006; Huggenberger and Regli, 2006). The presence of fine-grained S1 beds, interbedded with occasional S3 and S4 beds, is indicative of bioturbated channel-bar deposits or overbank deposits (Bridge, 1993; Bridge and Lunt, 2006). Tractionstructured conglomerate beds (G1) (Fig. 4F) represent channel-fill deposition during periods of higher flow velocity in the deepest active channels. Bed thicknesses indicate channel depths of at least 1 m (Gibling, 2006). Therefore, we interpret lithofacies S1-S4 and G1 to represent deposition in a sand-dominated braided river system with substantial volcaniclastic input (Fig. 4A; Miall, 1977; Cant and Walker, 1978; Walker and Cant, 1984; Bridge, 1993; Skelly et al., 2003; Bridge and Lunt, 2006; Huggenberger and Regli, 2006) based on the prevalence of midchannel bar morphologies, composed of S3 with fining-up sequences, overlain by S2 and S4, and channelfill bed morphologies, composed of S3 and G1 with basal scour surfaces.

A basin-wide transition to lacustrine-dominated deposition occurred at ca. 46 Ma (Fig. 4A). Gradual ponding of the preexisting drainage is

recorded by an up-section shift from channelized fluvial sandstones (S3–S5) and conglomerate (G1 and G2) beds to interbedded fossiliferous limestone (S6^A), finely laminated, organic-poor mudstone (M2), and gastropod grainstone (S6^B) beds (Fig. 4A, 80–340 m; Figs. S5–S7). The majority of the strata in the upper part of the Muddy Creek Basin (Fig. 2, map units Tos and Tcs) record a freshwater to moderately evaporative lacustrine system that fluctuated between the fluvial-lacustrine (overfilled) lithofacies associations and fluctuating-profundal (balanced-filled) lithofacies associations (Carroll and Bohacs, 1999; Bohacs et al., 2000) with occasional interbedded fluvial lithofacies (Fig. 4A).

Overfilled lacustrine deposition (Olsen, 1990; Carroll and Bohacs, 1999; Bohacs et al., 2000) is represented by M1 interbedded with beds of S2–S5, G1, and occasional beds of S6 (Fig. 4A; 440–600 m). Organic-rich mudstone (M1) represents lake-bottom deposition in a stratified lake where dysoxic bottom waters allowed for preservation of carbonaceous material (Olsen, 1990). Limestone and gastropod packstone (S6) beds and algal mats (Fig. S11, 34 m) suggest deposition within the littoral or sublittoral zone in a

carbonate shoal (Carroll and Bohacs, 1999; Tänavsuu-Milkeviciene and Sarg, 2012). G1 beds are commonly interbedded with M1 and S2–S5 beds and are most likely the result of fluvial channel deposition in the lake during lowstands, or progradation of the fluvial system (Tänavsuu-Milkeviciene and Sarg, 2012). Increasingly up section, fluvial strata contain greater amounts of preserved biota, including gastropods, ostracods, fish scales, insects, and terrestrial mammal bone fragments (Fig. 4A).

Periods of balanced-fill lake deposition (Carroll, 1998; Carroll and Bohacs, 1999; Bohacs et al., 2000; Graf et al., 2015) are represented by large packages of organic-poor mudstone with rare gastropods (M2) interbedded with ripple laminated sandstone beds (S5) and bentonite (Fig. 4A, 340–440 m and 600–780 m). Ripple laminated sandstone (S5) records turbidity currents or hyperpycnal flows that reached the deeper portions of the lake.

Sediment Provenance

Provenance indicators in the strata of the Muddy Creek Basin, including clast composi-

tions in conglomerates and detrital zircon U-Pb grain age peaks, show both regional and local sediment sourcing. While conglomerates outcrops are rare (Fig. 4A; Figs. S4-S12), clasts from lower group sample MT20-468MC (G2^B) (Figs. 2 and 4A, sample A) are predominantly tuff clasts, likely regionally sourced from the Challis volcanic field, exposed to the west of the basin (Janecke and Snee, 1993; M'Gonigle and Dalrymple, 1996; Chetel et al., 2011). Stratigraphically higher in the basin strata, in upper group samples MT21-539MC and MT21-553MC (Figs. 2 and 4A, samples D and F, respectively), clasts were predominantly gray and brown quartzites, tan siltstone, and rare tuff clasts. Quartzite clasts were likely sourced from the Upper Cretaceous to Lower Tertiary Beaverhead Conglomerate, siltstones are likely from the Permian Phosphoria Formation and Devonian Three Forks Formation exposed in the footwall along the Muddy Creek detachment fault, and tuff clasts are reworked Challis volcaniclastics (Janecke et al., 1999; Chetel et al., 2011; Scarberry et al., 2019). Localized sourcing of conglomerates agrees with extensive petrofacies analysis conducted by Janecke et al. (1999), where intrabasinal source regions from both the hanging wall and footwall were split into four distinct regions to explain progressive changes in provenance up section.

Detrital zircon U-Pb grain age peaks in lower group samples (Fig. 5A) are dominated by regional, westerly sourced grain age peaks at 49-48 Ma and 70 Ma. A detrital zircon age peak at 49-48 Ma was likely sourced from the Challis volcanic field to the west of the Muddy Creek Basin (Janecke and Snee, 1993; M'Gonigle and Dalrymple, 1996; Chetel et al., 2011), and detrital zircon age peaks between 70 Ma and 68 Ma were likely derived from the Atlanta peraluminous suite of the Idaho Batholith (Figs. 1 and 5A; Gaschnig et al., 2010). Grain age peaks at 432 Ma, 1160 Ma, and 1500 Ma from upper group samples match closely with prominent age peaks within the Pennsylvanian Quadrant Formation and the Permian Phosphoria and Park City Formations, which are locally exposed in the footwall of the eastern detachment fault in the Tendoy Mountains (Fig. 2; Schwartz et al., 2019; Ronemus et al., 2021). The 1160 Ma detrital zircon age peak could also be explained by the Mississippian Kibbey and Snowcrest Sandstone Formations bounding the western portion of the basin (Ronemus et al., 2021). Due to the thin nature of these beds and the majority of the Mississippian sedimentary strata being composed of limestone, this time period is likely underrepresented in the zircon provenance record (Ronemus et al., 2021). Age peaks between 1800 Ma and 1600 Ma were likely

sourced from the Prichard Group and Upper Belt strata (Link et al., 2016), or from recycled Belt Supergroup units in Mississippian—Permian strata (Schwartz et al., 2019). While it is difficult to constrain the exact provenance of potentially multicyclic recycled grains by a single U-Pb age, previously published clast counts (Janecke et al., 1999) and new clast composition data described in the lithofacies descriptions support localized sediment sourcing from Paleozoic sedimentary strata exposed in the hanging wall and footwall of the Muddy Creek Basin.

DISCUSSION

Basin Evolution

The evolution of the Muddy Creek Basin allows us to better understand landscape and paleodrainage evolution in Montana, Idaho, and Wyoming during Eocene time. Overall, we found that age data from the three chronologic methods presented here are internally consistent with their respective positions in the stratigraphy (Fig. 3) and indicate basin deposition from 49 Ma to at least 36 Ma. Depositional ages become younger moving south through the basin (Figs. 2 and 3; Table 1), indicating a southward shift of depositional center from 47 Ma onward. This agrees with the interpretations of Janecke et al. (1999), which stated that movement along the bounding detachment fault became younger to the south. Integrating the stratigraphic, geochronologic, and thermochronologic data presented above, we outline the detailed evolution of the Muddy Creek Basin for four separate time intervals: 60-50 Ma, 49-47 Ma, 46.9-37 Ma, and post-37 Ma.

T1: Early Paleogene to Early Eocene (60–50 Ma)

Prior to the start of Muddy Creek Basin deposition, the region acted as part of the Cretaceous Lemhi Pass paleovalley that flowed from the Salmon River Mountains across southwest Montana through the active Sevier fold-andthrust front (Fig. 1), eventually depositing the Harbell-Pinyon megafan during latest Cretaceous times, and then delivering Challis volcanic field-derived sediment to the Green River Basin in western Wyoming from ca. 49 Ma to 47 Ma (Fig. 6A; Janecke et al., 2000; Smith et al., 2008; Chetel et al., 2011). The existence of this paleovalley is supported by quartzite and rapakivi granite clasts found within the Harbell-Pinyon conglomerate sourced from the Salmon River Mountains (Fig. 6A), and detailed mapping of ignimbrite flows confined within the margins of the paleovalley (Janecke et al., 2000). No known active extension occurred in this region prior to 50 Ma (Vogl et al., 2012; Howlett et al., 2021), but 150 km north in western Montana, thermochronologic data indicate that both the Anaconda and Bitterroot metamorphic core complexes were undergoing extension by 53 Ma (Fig. 3; Foster and Asaf, 2002; House et al., 2002; Foster et al., 2010; Whitney et al., 2013).

T2: Early Eocene (49–47 Ma)

Challis ignimbrite volcanism began by at least 49.78 ± 0.31 Ma (Figs. 1 and 3; M'Gonigle and Dalrymple, 1996; Janecke et al., 1999; Janecke and Blankenau, 2003), and possibly as early as 52 Ma (Stroup et al., 2008; Chetel et al., 2011). Sanidine and feldspar ⁴⁰Ar/³⁹Ar dating of Challis ignimbrites and volcaniclastic sandstones in the Green River Basin (GRB; Fig. 1) show that Challis sediment was being delivered to the Green River Basin as early as 49 Ma (Smith et al., 2008; Chetel et al., 2011). Sandstone samples 06FR86 and 05CP1 from Chetel et al. (2011), which were deposited prior to 48.95 ± 0.29 Ma, based on two overlying Challis tuffs, have Challis volcanic field-sourced detrital feldspar grain ages between 52.26 ± 0.50 Ma and 48.97 ± 0.12 Ma (Smith et al., 2008; Chetel et al., 2011). The presence of these Challis volcanic field-sourced detrital feldspar grains suggests that Challis sediment was traveling through the Lemhi Pass paleovalley into the Green River Basin prior to 48.4 Ma (Fig. 6A). Muddy Creek Basin deposition began ca. 49 Ma with the emplacement of multiple ignimbrites in the northwest corner of the basin, based on new sanidine 40Ar/39Ar dates from the basal portion of the sedimentary section (Fig. 2), which range from $48.40 \pm 0.05 \,\mathrm{Ma}$ to $48.15 \pm 0.05 \,\mathrm{Ma}$ (Table 2; Fig. 6B), and previous work indicating $^{40}\text{Ar}/^{39}\text{Ar}$ ages of 47 ± 0.16 Ma and 49.47 ± 0.05 Ma (M'Gonigle and Dalrymple, 1996; Janecke et al., 1999). These ignimbrites likely flowed south/southeast from the Challis volcanic field through the Lemhi Pass paleovalley into the basin (Fig. 6B), based on previous mapping and lithologic correlations (M'Gonigle and Dalrymple, 1996; Janecke et al., 2000). The presence of Challis volcanic field-sourced material in the Green River Basin for \sim 500 k.y. prior to initiation of deposition in the Muddy Creek Basin (Smith et al., 2008; Chetel et al., 2011) suggests continued transport of sediment through the Lemhi Pass paleovalley during a period of high sediment influx during active Challis volcanism (Fig. 6A). Challis volcanic field-derived sediment continued to be delivered to the Green River Basin from 49 Ma to 47 Ma, signaling that, prior to the start of Muddy Creek deposition, high sediment influx was not forcing in-valley sediment deposition (Janecke et al., 1999; Chetel et al., 2011). Instead, we favor ini-

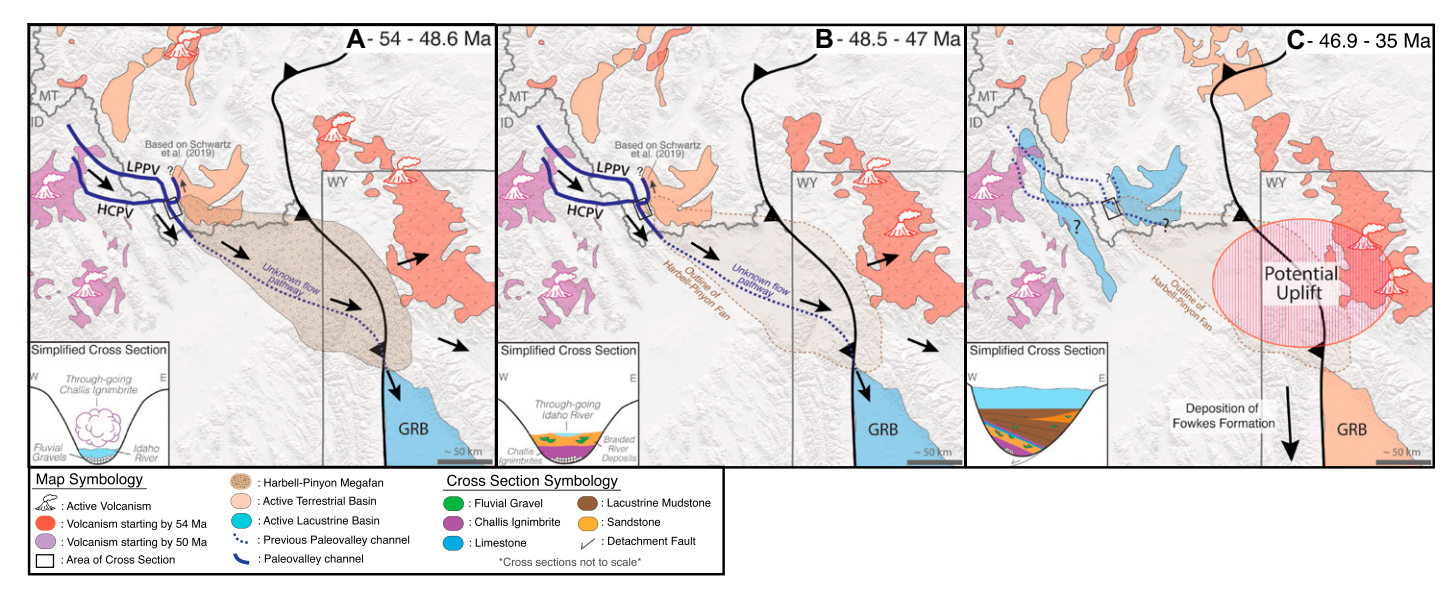


Figure 6. Paleogeographic reconstruction of southwest Montana, southeast Idaho, and western Wyoming from early Eocene to late Eocene time with simplified cross sections of the Muddy Creek Basin. Black arrows indicate sediment transport direction (Chetel et al., 2011). (A) Early Eocene time (Janecke et al., 2000; Schwartz et al., 2019). (B) Mid-Eocene time. (C) Mid-Eocene to late Eocene. Potential area of uplift is sourced from Smith et al. (2008). Mapped volcanics and basins are sourced from Constenius (1996), Smith et al. (2008), and Vuke (2020). Small black rectangle represents location of Figure 2. GRB—Green River Basin; HCPV—Hawley Creek paleovalley; ID—Idaho; LPPV—Lemhi Pass paleovalley; MT—Montana; WY—Wyoming.

tiation of basin deposition in relation to localized subsidence. Thermal extensional reactivation of Sevier thrust structures at depth (Janecke et al., 1999) is a potential driver for subsidence, and the location correlates with previous interpretations of initial extension ca. 49 Ma along the northern portion of the Muddy Creek detachment fault, adjacent to the location of dated Challis-derived sediment deposited within the basin (Fig. 2, units Tccg and Tcbs; Dunlap, 1982; Janecke et al., 1999).

Following Challis ignimbrite deposition in the Muddy Creek Basin, the 34-m-thick tuffaceous fluvial sequence was deposited in less than 2 m.y. (Figs. 3 and 4). Grain ages and clast compositions within this section show that the fluvial system reworked previously deposited Challis volcanic field—sourced volcaniclastics, along with input from the Salmon River Mountains (Janecke et al., 1999, 2000). South-directed paleocurrents (Fig. 3) are consistent with transport of sediment in a similar direction to the previous paleovalley (Fig. 2, inset; Janecke et al., 2000).

T3: Middle to Late Eocene (46.9–37 Ma)

The basal Muddy Creek fluvial sequence is capped by a 46.8 ± 0.05 Ma Challis ignimbrite (Table 2, sample 4), and 4 m of fossiliferous limestone containing gastropods and shelly debris (Fig. 4E). This interval records the first instance of basin ponding, coinciding temporally with the cessation of delivery of Challis volca-

nic field sediment into the Green River Basin at 47 Ma (Fig. 6C; Smith et al., 2008; Chetel et al., 2011). Following initial basin ponding, thick packages of lacustrine mud (M1 and M2) with interbedded ripple laminated sandstone (S5) and fossiliferous limestone (S6) become more prominent as the environment shifted from fluvial to freshwater lacustrine. This transition occurred between 46.8 Ma and 40.4 Ma, based on two maximum depositional ages of 43.01 ± 0.97 Ma and 40.4 ± 0.48 Ma (Table 1, samples MT21-549MC and MT20-474MC). This lithofacies shift was not accompanied by a change in provenance, with strata dominated by U-Pb grain age components indicative of westerly sources including the Challis volcanic field and the Atlanta peraluminous suite of the Idaho Batholith throughout the lower part of the section (Fig. 5A, lower group samples). Zircon (U-Th)/He cooling ages from the lower group samples range from 54 Ma to 41 Ma, also supporting westerly sourcing (Fig. 5B, lower group analyses). These ZHe cooling ages are likely volcanic in nature, as ages match those from the Challis volcanic field and the youngest detrital zircon grain ages (Fig. 1). Previous studies have attributed initial basin ponding to extension (Janecke et al., 1999; Janecke, 2007), but the similarities in sediment provenance and ZHe cooling ages within the basin strata across this sharp basin-wide lithofacies transition suggest the need for an additional regional driver. The correlation in timing between basin ponding and the end of Challis volcaniclastic sediment input into the Green River Basin at 47.1 Ma (Smith et al., 2008; Chetel et al., 2011), and with the southward propagation of Absaroka Province volcanism (Hiza, 1999) provides a regional driver for backfilling and basin ponding due to thermal uplift and/or isostatic uplift east of the Muddy Creek Basin, along the Sevier thrust front and the Absaroka volcanic field (Fig. 6C). Both global and local available isotopic records show climatic stability and limited variation in δ¹⁸O values during this transition, so we favor a tectonic driver interpretation for basin ponding (Methner, 2016; Schwartz et al., 2019; Westerhold et al., 2020).

T4: Late Eocene (37 to ca. 34 Ma)

Continued lithospheric thermal weakening from active volcanism in the Dillon volcanic field (Fig. 1) and extensional reactivation of Sevierstyle thrust structures initiated surface-breaking extensional deformation in the Muddy Creek Basin starting ca. 37 Ma. Basin strata become coarser with an increase in the frequency of fluvial sandstone and conglomerate beds within lacustrine mudstone sections (Figs. 4A and 6C). Increased sandstone and conglomerate input is indicative of lake-level fluctuations and greater fluvial/deltaic input into the basin. One explanation for this lithofacies change is increasing aridity driving more seasonal evaporation; increasing δ^{13} C values in soil carbonates in the upper part of the basin section have been interpreted

as recording a period of aridification throughout western Montana (Methner, 2016; Schwartz et al., 2019). While this could have played a role in Muddy Creek Basin sedimentation, strata continue to be dominated by organic-rich mudstone with abundant organic matter, including gastropods and bivalves, and with limited calcic paleosol development (Fig. 4E) and no indications of evaporative or underfilled lacustrine deposition, indicating the continued dominance of a freshwater lacustrine system (Figs. 3 and 4A). It is more likely that these increases in fluvial interbeds and lake-level fluctuations were responses to the initiation of surface-breaking extension, exhuming Paleozoic basement along the eastern Muddy Creek detachment fault (Fig. 2). Motion along the detachment fault would have created relief and increased erosion, providing a flux of local sediment into the basin (Fig. 3). A shift in provenance correlates with this shift in lithofacies. Clastic sediments in this part of the section show west-directed paleocurrents and basement-derived detrital zircon grain age signatures (Fig. 5A, upper group samples). Detrital zircon U-Pb components are dominated by age peaks at 432 Ma, 1163 Ma, and 1800-1500 Ma (Fig. 5A), consistent with derivation from Paleozoic sedimentary strata exposed in the footwall of the detachment fault, which is supported by westerly paleocurrents (Fig. 3). Detrital zircon (U-Th)/He cooling ages shift from Eocene cooling ages to Paleozoic cooling ages, ranging from 422 Ma to 261 Ma (Fig. 5B). There is only 2-4 km of proposed total displacement along the Muddy Creek detachment fault (Janecke et al., 1999), indicating that there was not enough movement to exhume thermally reset grains, supporting local, easterly sourcing of the Paleozoic cooling ages.

Basin deposition continued through the late Eocene, until at least 36.0 ± 0.64 Ma, based on our stratigraphically youngest MDA (Table 1, sample MT21-553MC). Strata become coarser toward the top of basin. We interpret the increasing frequency of fluvial lithofacies in the upper portion of the Muddy Creek Basin as recording additional lake-level fluctuations and fluvial input from the footwall related to continuing extensional deformation. These fluvial strata are capped by additional organic-rich mudstone, indicating a return to freshwater lacustrine deposition, making solely climate-controlled basin aridification less likely. The section ends in an erosional unconformity. Although it remains unclear when deposition in the Muddy Creek Basin ended (Fig. 3), this study shows that the main phase of Muddy Creek Basin deposition was significantly older than previously hypothesized (Dunlap, 1982; Janecke et al., 1999; Methner, 2016).

Extension and Slab Removal

Identification of Eocene extension and basin subsidence in the Muddy Creek Basin during a phase of active extension and volcanism in Montana and Idaho (Janecke, 1994; Constenius, 1996: Janecke et al., 1999: House et al., 2002: Foster et al., 2010) allows us to put this basin record in the context of larger, cordilleran-scale deformation following well-constrained Sevier and Laramide compressional deformation. Previous work has attributed the majority of extension in western Montana to gravitational collapse of thermally weakened lithosphere (Coney and Harms, 1984; Constenius, 1996; Howlett et al., 2021), but this interpretation fails to explain the range of style, magnitude, and timing of extension we observed across the region (Janecke, 1994, 2007; Janecke et al., 1999; Foster and Asaf, 2002; Janecke and Blankenau, 2003; Foster et al., 2010; Howlett et al., 2021). Additionally, extension in this region has been crudely constrained within the context of Farallon slab rollback (Dickinson, 2004; Liu and Stegman, 2011; Smith et al., 2014). The surface expression of Farallon slab rollback has been interpreted as a southward sweep of extension and magmatism, accompanied by small-scale topographic change, starting in Montana and migrating to the southwest, following the general direction of Farallon slab retreat (e.g., Smith et al., 2014; Copeland et al., 2017; Cassel et al., 2018).

Bitterroot-Lowland Creek-Crazy Mountains. The Bitterroot and Anaconda metamorphic core complexes are interpreted to have begun extending ca. 53 Ma, coeval with the initial phases of Lowland Creek and northern Absaroka volcanism, forming the interpreted 53 Ma slab edge axis of Smith et al. (2014, see their fig. 1) (see also Fig. 1 herein; Hodges and Applegate, 1993; Foster et al., 2010; Fan and Carrapa, 2014; Hiza, 1999). Volcanism in the Crazy Mountains (MT) ca. 51-49 Ma and in the Black Hills (Wyoming-South Dakota) ca. 58-46 Ma has also been associated with mantle interactions at the edge of the Farallon slab, although this volcanism is also interpreted as resulting from slab window processes (Duke, 2009). Geochemical evidence from the Black Hills and the Missouri Breaks of central Montana shows an increased asthenospheric component in post-50 Ma magmas in comparison to pre-50 Ma magma (Duke, 2009), consistent with slab removal.

Challis–Muddy Creek–Laramide Foreland. From 53 Ma to 47 Ma, Farallon slab rollback progressed westward across the Laramide foreland, as documented by a series of basin ponding events followed by successive unconformity formation (Smith et al., 2014). Similarly, volcanism and basin subsidence progressed southward with the initiation of Challis volcanism ca. 50 Ma,

shortly followed by initiation of Muddy Creek Basin and Sage Creek Basin deposition (Fig. 1; Smith et al., 2008; Chetel et al., 2011; Schwartz et al., 2019). The results presented here show that Muddy Creek Basin subsidence initiated at ca. 49 Ma, allowing for the deposition of the basal tuffaceous fluvial sequence, which continued until 46.8 Ma, when initial basin ponding occurred.

Ruby Mountains–Elko Basin. Volcanism progressed to the southwest, arriving in northeastern Nevada ca. 44 Ma (Henry et al., 2011), and extension initiated in the Ruby Mountains–East Humboldt metamorphic core complex at 45 Ma and accelerated at 43 Ma (Canada et al., 2020). The onset of subsidence in the Elko Basin began at ca. 44 Ma with the deposition of a basal tuffaceous fluvial/alluvial sequence, followed by basin ponding and expansion at 43 Ma (Canada et al., 2020). The basin sequence is capped by an influx of volcanic ignimbrites at 40.5 Ma, and volcanism migrated southwestward to central Nevada by 35 Ma (Canada et al., 2021; Henry et al., 2011).

This southwestward progression of volcanism, extension, and basin ponding, including this new record from the Muddy Creek Basin, fits within the preserved surface record of Farallon slab rollback (and possible lower lithosphere delamination; Canada et al., 2021), expanding our understanding of the mantle dynamics involved in slab rollback and the ways in which these dynamics are preserved in the surface record. The continuation of basin subsidence and deposition after the passage of the volcanic and extensional front associated with slab removal remains a fundamental difference between the basins in southwestern Montana, exemplified by the Muddy Creek Basin, and the Laramide foreland and Elko Basins.

CONCLUSIONS

- (1) Basal deposition in the Muddy Creek Basin is represented by tuffaceous sandstone and conglomerate in a sandy braided river system, which reworked previously deposited Challis volcaniclastic material, interbedded with Challis volcanic field–sourced ignimbrites. Deposition transitioned to a lacustrine environment with overfilled lithofacies associations, and interbedded fluvial tongues representing lake-level fluctuations. Basin strata are capped by fluvial conglomerates overlain by additional lacustrine mudstones.
- (2) Detrital zircon maximum depositional ages and sanidine ⁴⁰Ar/³⁹Ar dating of Challis ignimbrites constrain the deposition of basal tuffaceous fluvial strata to between 48.5 Ma and 46 Ma. Basin strata transition from fluvial to

lacustrine deposition between 46 Ma and 40 Ma, with strata representing full lacustrine deposition by 40 Ma. An increase in fluvial input into the paleolake occurred at 36 Ma. Basin deposition ended sometime after 36 Ma, with the precise end of deposition remaining unconstrained, calling for further work in the Muddy Creek Basin.

- (3) Detrital zircon U-Pb and (U-Th)/He provenance data and clast compositions indicate regional sourcing from the Challis volcanic field and the Idaho Batholith from ca. 48.5 Ma to 40 Ma. A transition occurred between 40 Ma and 36 Ma from regional to locally sourced sediment, with source areas including Paleozoic sedimentary strata exposed in the footwall of the Muddy Creek detachment fault. We interpret this shift in provenance to represent the initiation of surface-breaking extension.
- (4) Initial basin subsidence at 48.5 Ma was a result of thermal extensional reactivation of previous Sevier structures. Basin ponding at 46.8 Ma is attributed to paleodrainage reorganization as a result of both thermal and/or isostatic uplift east of the basin in the Sevier fold-andthrust belt front and continued localized basin subsidence related to thermal weakening. Surface-breaking extension began ca. 37 Ma, based on a shift to localized sediment provenance, westerly paleocurrents, and an increased frequency of sandstone and conglomerate interbeds, and it is attributed to continued thermal weakening of Sevier-style contractional features and continued evolution of the Muddy Creek detachment fault, allowing the fault to reach the surface.
- (5) Our new record of Muddy Creek Basin deposition and subsidence helps to further constrain the surface record of Farallon slab rollback, as the timing of basin ponding, extension, and local volcanism fits within the geochronologic constraints and basin facies model associated with the southwestward progression of the slab and/or lower lithospheric mantle removal. Differences in the longevity of basin subsidence may relate to preexisting lithospheric conditions.

ACKNOWLEDGMENTS

This work is supported by National Science Foundation CAREER grant EAR-1848563 to Cassel, and student grants to Thoresen from the Geological Society of America, American Association of Petroleum Geologists, Society for Sedimentary Geology, Rocky Mountain Association of Geologists, Society of Economic Geologists, Tobacco Root Geological Society, and the University of Idaho College of Science and Graduate and Professional Association. This material is also based upon work supported by the National Science Foundation under grants EAR-1759200 and EAR-1759353 to the AGeS program. Any opinions indings, and conclusions or recommendations expressed in this material are those of the author(s) and do not necessarily reflect the views of the National

Science Foundation. Thank you to the AGeS program for its support. This work greatly benefited from conversations with C. Elliot and J. Stanley, as well as field assistance from L. Basler, C. Peever, J. Martin, E. Young-Dahl, and N. Usachenko. We also extend our gratitude to L. Stockli, R. Chatterjee, J. Fosdick, and M. Mueller for laboratory assistance. The Basin Analysis & Helium Thermochronology Laboratory (BAHTL) is supported by National Science Foundation grant EAR-735492 to Fosdick. We extend our gratitude to Theresa Schwartz, Peter Druschke, and the associate editor, Robinson Cecil, for providing detailed reviews that significantly improved the paper.

REFERENCES CITED

- Ault, A.K., Gautheron, C., and King, G.E., 2019, Innovations in (U-Th)/He, fission track, and trapped charge thermochronometry with applications to earthquakes, weathering, surface-mantle connections, and the growth and decay of mountains: Tectonics, v. 38, p. 3705–3739, https://doi.org/10.1029/2018TC005312.
- Bendick, R., and Baldwin, J., 2009, Dynamic models for metamorphic core complex formation and scaling: The role of unchannelized collapse of thickened continental crust: Tectonophysics, v. 477, p. 93–101, https://doi.org/ /10.1016/j.tecto.2009.03.017.
- Bohacs, K.M., Carroll, A.R., Neal, J.E., and Mankiewicz, P.J., 2000, Lake-basin type, source potential, and hydrocarbon character: An integrated sequence-stratigraphic–geochemical framework, in Gierlowski-Kordesch, E.H., and Kelts, K.R., eds., Lake Basins through Space and Time: American Association of Petroleum Geologists Studies in Geology 46, p. 3–34, https://doi.org/10 .1306/St46706C1.
- Bridge, J.S., 1993, The interaction between channel geometry, water flow, sediment transport and deposition in braided rivers, in Best, J.L., and Bristow, C.S., eds., Braided Rivers: Geological Society, London, Special Publication 75, p. 13–71, https://doi.org/10.1144/GSL.SP.1993.075.01.02.
- Bridge, J.S., and Lunt, I.A., 2006, Depositional models of braided rivers, in Jarvis, I., Sambrook Smith, G.H., Best, J.L., Bristow, C.S., and Petts, G.E., eds., Braided Rivers: Process, Deposits, Ecology, and Management: New York, Wiley, p. 11–50, https://doi.org/10.1002/9781444304374 cb2
- Canada, A.S., Cassel, E.J., Stockli, D.F., Smith, M.E., Jicha, B.R., and Singer, B.S., 2020, Accelerating exhumation in the Eocene North American Cordilleran hinterland: Implications from detrital zircon (U-Th)/(He-Pb) double dating: Geological Society of America Bulletin, v. 132, p. 198–214, https://doi.org/10.1130/B35160.1.
- Canada, A.S., Cassel, E.J., and Smith, M.E., 2021, Geochemical evolution of Eocene lakes in the Nevada hinterland of the North American Cordillera: Geochemistry, Geophysics, Geosystems, v. 22, https://doi.org/10.1029/2021.GC009863
- Cant, D.J., and Walker, R.G., 1978, Fluvial processes and facies sequences in the sandy braided South Saskatchewan River, Canada: Sedimentology, v. 25, p. 625–648, https://doi.org/10.1111/j.1365-3091.1978.tb00323.x.
- Carrapa, B., DeCelles, P.G., and Romero, M., 2019, Early inception of the Laramide orogeny in southwestern Montana and northern Wyoming: Implications for models of flat-slab subduction: Journal of Geophysical Research: Solid Earth, v. 124, p. 2102–2123, https://doi.org/10.1029/2018JB016888.
- Carroll, A.R., 1998, Upper Permian lacustrine organic facies evolution, Southern Junggar Basin, NW China: Organic Geochemistry, v. 28, p. 649–667, https://doi.org/10.1016/S0146-6380(98)00040-0.
- Carroll, A.R., and Bohaes, K.M., 1999, Stratigraphic classification of ancient lakes: Balancing tectonic and climatic controls: Geology, v. 27, p. 99–102, https://doi.org/10.1130/0091-7613(1999)027<0099:SCOALB>2 3.CO:2.
- Cassel, E.J., Smith, M.E., and Jicha, B.R., 2018, The impact of slab rollback on Earth's surface: Uplift and extension in the hinterland of the North American Cordillera:

- Geophysical Research Letters, v. 45, p. 10,996–11,004, https://doi.org/10.1029/2018GL079887.
- Chetel, L.M., Janecke, S.U., Carroll, A.R., Beard, B.L., Johnson, C.M., and Singer, B.S., 2011, Paleogeographic reconstruction of the Eocene Idaho River, North American Cordillera: Geological Society of America Bulletin, v. 123, p. 71–88, https://doi.org/10.1130/B30213.1.
- Colgan, J.P., Dumitru, T.A., Reiners, P.W., Wooden, J.L., and Miller, E.L., 2006, Cenozoic tectonic evolution of the Basin and Range Province in northwestern Nevada: American Journal of Science, v. 306, p. 616–654, https://doi.org/10.2475/08.2006.02.
- Coney, P.J., 1987, The regional tectonic setting and possible causes of Cenozoic extension in the North American Cordillera, in Coward M.P., Dewey, J.F., and Hancock, P.L., eds., Continental Extensional Tectonics: Geological Society, London, Special Publication 28, p. 177– 186, https://doi.org/10.1144/GSL.SP.1987.028.01.13.
- Coney, P.J., and Harms, T.A., 1984, Cordilleran metamorphic core complexes: Cenozoic extensional relics of Mesozoic compression: Geology, v. 12, p. 550–554, https://doi.org/10.1130/0091-7613(1984)12<550: CMCCCE>2.0.CO:2.
- Constenius, K.N., 1996, Late Paleogene extensional collapse of the Cordilleran foreland fold and thrust belt: Geological Society of America Bulletin, v. 108, p. 20–39, https://doi.org/10.1130/0016-7606(1996)108<0020: LPECOT>2.3.CO;2.
- Cooperdock, E.H.G., Ketcham, R.A., and Stockli, D.F., 2019, Resolving the effects of 2-D versus 3-D grain measurements on apatite (U-Th)/He age data and reproducibility: Geochronology, v. 1, p. 17–41, https:// doi.org/10.5194/gchron-1-17-2019.
- Copeland, P., Currie, C.A., Lawton, T.F., and Murphy, M.A., 2017, Location, location, location: The variable lifespan of the Laramide orogeny: Geology, v. 45, p. 223– 226, https://doi.org/10.1130/G38810.1.
- Currie, B.S., 2002, Structural configuration of the Early Cretaceous Cordilleran foreland-basin system and Sevier thrust belt, Utah and Colorado: The Journal of Geology, v. 110, p. 697–718, https://doi.org/10.1086/342626.
- DeCelles, P.G., 1994, Late Cretaceous-Paleocene synorogenic sedimentation and kinematic history of the Sevier thrust belt, northeast Utah and southwest Wyoming: Geological Society of America Bulletin, v. 106, p. 32–56, https://doi.org/10.1130/0016-7606(1994)106<0032:LCPSSA>2.3.CO;2.
- DeCelles, P.G., 2004, Late Jurassic to Eocene evolution of the Cordilleran thrust belt and foreland basin system, western U.S.A.: American Journal of Science, v. 304, p. 105–168, https://doi.org/10.2475/ajs.304.2.105.
- Dickinson, W.R., 2004, Evolution of the North American Cordillera: Annual Review of Earth and Planetary Sciences, v. 32, p. 13–45, https://doi.org/10.1146/annurev .earth.32.101802.120257.
- Dickinson, W.R., and Gehrels, G.E., 2009, Use of U-Pb ages of detrital zircons to infer maximum depositional ages of strata: A test against a Colorado Plateau Mesozoic database: Earth and Planetary Science Letters, v. 288, p. 115–125, https://doi.org/10.1016/j.epsl.2009.09.013.
- Druschke, P., Hanson, A.D., Wells, M.L., Gehrels, G.E., and Stockli, D., 2011, Paleogeographic isolation of the Cretaceous to Eocene Sevier hinterland, east-central Nevada: Insights from U-Pb and (U-Th)/He detrital zircon ages of hinterland strata: Geological Society of America Bulletin, v. 123, p. 1141–1160, https://doi.org/10.1130/B30029.1.
- Dudás, F.Ö., Ispolatov, V.O., Harlan, S.S., and Snee, L.W., 2010, ⁴⁰Arf⁵⁹Ar geochronology and geochemical reconnaissance of the Eocene Lowland Creek volcanic field, west-central Montana: The Journal of Geology, v. 118, p. 295–304, https://doi.org/10.1086/651523.
- Duke, G.I., 2009, Black Hills–Alberta carbonatite-kimber-lite linear trend: Slab edge at depth?: Tectonophysics, v. 464, p. 186–194, https://doi.org/10.1016/j.tecto.2008.09.034.
- Dunlap, D.G., 1982, Tertiary geology of the Muddy Creek Basin, Beaverhead County, Montana [M.S. thesis]: Missoula, Montana, University of Montana, 146 p.
- Fan, M., and Carrapa, B., 2014, Late Cretaceous–early Eocene Laramide uplift, exhumation, and basin subsidence in Wyoming: Crustal responses to flat slab sub-

- duction: Tectonics, v. 33, p. 509–529, https://doi.org/10 .1002/2012TC003221.
- Fields, R.W., Rasmussen, D.L., Tabrum, A.R., and Nichols, R., 1985, Cenozoic rocks of the intermontane basins of western Montana and eastern Idaho: A summary, in Flores, R.M., and Kaplan, S.S., eds., Cenozoic Paleogeography of the West-Central United States: Denver, Colorado, Rocky Mountain Section, Society of Economic Paleontologists and Mineralogists (SEPM), p. 9–36.
- Foster, D.A., and Asaf, R., 2002, Low-temperature thermochronological record of exhumation of the Bitterroot metamorphic core complex, northern Cordilleran orogen: Tectonophysics, v. 349, p. 23–36, https://doi.org /10.1016/S0040-1951(02)00044-6.
- Foster, D.A., Grice, W.C., and Kalakay, T.J., 2010, Extension of the Anaconda metamorphic core complex: ⁴⁰Arf³⁹Ar thermochronology and implications for Eocene tectonics of the northern Rocky Mountains and the Boulder Batholith: Lithosphere, v. 2, p. 232–246, https://doi.org /10.1130/L94.1.
- Fritz, W.J., and Sears, J.W., 1993, Tectonics of the Yellowstone hotspot wake in southwestern Montana: Geology, v. 21, p. 427–430, https://doi.org/10.1130/0091-7613(1993)021<0427:TOTYHW>2.3.CO;2.
- Fritz, W.J., Sears, J.W., McDowell, R.J., and Wampler, J.M., 2007, Cenozoic volcanic rocks of southwestern Montana: Northwest Geology, v. 36, p. 91–110.
- Fuentes, F., DeCelles, P.G., Constenius, K.N., and Gehrels, G.E., 2011, Evolution of the Cordilleran foreland basin system in northwestern Montana, U.S.A.: Geological Society of America Bulletin, v. 123, p. 507–533, https:// doi.org/10.1130/B30204.1.
- Gaschnig, R.M., Vervoort, J.D., Lewis, R.S., and McClelland, W.C., 2010, Migrating magmatism in the northern US Cordillera: In situ U-Pb geochronology of the Idaho Vatholith: Contributions to Mineralogy and Petrology, v. 159, p. 863–883, https://doi.org/10.1007/s00410-009-0459-5.
- Gehrels, G., 2014, Detrital zircon U-Pb geochronology applied to tectonics: Annual Review of Earth and Planetary Sciences, v. 42, p. 127–149, https://doi.org/10.1146/annurev-earth-050212-124012.
- Gibling, M.R., 2006, Width and thickness of fluvial channel bodies and valley fills in the geological record: A literature compilation and classification: Journal of Sedimentary Research, v. 76, p. 731–770, https://doi .org/10.2110/jsr.2006.060.
- Graf, J.W., Carroll, A.R., and Smith, M.E., 2015, Lacustrine sedimentology, stratigraphy and stable isotope geochemistry of the Tipton Member of the Green River Formation, in Smith, M.E., and Carroll, A.R., eds., Stratigraphy and Paleolimnology of the Green River Formation, Western USA: Dordrecht, Netherlands, Springer Syntheses in Limnogeology, p. 31–60, https://doi.org /10.1007/978-94-017-9906-5
- Guenthner, W.R., Reiners, P.W., Ketcham, R.A., Nasdala, L., and Giester, G., 2013, Helium diffusion in natural zircon: Radiation damage, anisotropy, and the interpretation of zircon (U-Th)/He thermochronology: American Journal of Science, v. 313, p. 145–198, https://doi.org /10.2475/03.2013.01.
- Hanneman, D.L., 1989, Cenozoic Basin Evolution in a Part of Southwestern Montana: Missoula, Montana, University of Montana, 205 p.
- Hanneman, D.L., and Wideman, C.J., 1991, Sequence stratigraphy of Cenozoic continental rocks, southwestern Montana: Geological Society of America Bulletin, v. 103, p. 1335–1345, https://doi.org/10.1130 //0016-7606(1991)103
- Hart, N.R., Stockli, D.F., Lavier, L.L., and Hayman, N.W., 2017, Thermal evolution of a hyperextended rift basin, Mauléon Basin, western Pyrenees: Tectonics, v. 36, p. 1103–1128, https://doi.org/10.1002/2016TC004365.
- Henry, C.D., 2008, Ash-flow tuffs and paleovalleys in north-eastern Nevada: Implications for Eocene paleogeography and extension in the Sevier hinterland, northern Great Basin: Geosphere, v. 4, p. 1–35, https://doi.org/10.1130/GES00122.1.
- Henry, C.D., McGrew, A.J., Colgan, J.P., Snoke, A.W., and Brueseke, M.E., 2011, Timing, distribution, amount, and style of Cenozoic extension in the northern Great

- Basin, *in* Lee, J., and Evans, J.P., eds., Geologic Field Trips to the Basin and Range, Rocky Mountains, Snake River Plain, and Terranes of the U.S. Cordillera: Geological Society of America Field Guide 21, p. 27–66, https://doi.org/10.1130/2011.0021(02).
- Hiza, M.M., 1999, The geochemistry and geochronology of the Eocene Absaroka volcanic province, northern Wyoming and southwest Montana, United States of America [Ph.D. thesis]: Corvallis, Oregon, Oregon State University, 243 p.
- Hodges, K.V., and Applegate, J.D., 1993, Age of Tertiary extension in the Bitterroot metamorphic core complex, Montana and Idaho: Geology, v. 21, p. 161–164, https://doi.org/10.1130/0091-7613(1993)021<0161: AOTEIT>2.3.CO;2.
- House, M.A., Bowring, S.A., and Hodges, K.V., 2002, Implications of middle Eocene epizonal plutonism for the unroofing history of the Bitterroot metamorphic core complex, Idaho-Montana: Geological Society of America Bulletin, v. 114, p. 448–461, https://doi.org/10.1130/0016-7606(2002)114<0448:IOMEEP>2.0.CO;2.
- Howlett, C.J., Reynolds, A.N., and Laskowski, A.K., 2021, Magmatism and extension in the Anaconda metamorphic core complex of western Montana and relation to regional tectonics: Tectonics, v. 40, https://doi.org/10 .1029/2020TC006431.
- Huggenberger, P., and Regli, C., 2006, A sedimentological model to characterize braided river deposits for hydrogeological applications, in Jarvis, I., Sambrook Smith, G.H., Best, J.L., Bristow, C.S., and Petts, G.E., eds., Braided Rivers: Process, Deposits, Ecology, and Management: New York, Wiley, p. 51–74, https://doi.org/10 .1002/9781444304374.ch3.
- Humphreys, E., 1995, Post-Laramide removal of the Farallon slab, western United States: Geology, v. 23, p. 987–990, https://doi.org/10.1130 /0091-7613(1995)023<0987:PLROTF>2.3.CO;2.
- Humphreys, E., 2009, Relation of flat subduction to magmatism and deformation in the western United States, in Kay, S.M., Ramos, V.A., and Dickinson, W.R., eds., Backbone of the Americas: Shallow Subduction, Plateau Uplift, and Ridge and Terrane Collision: Geological Society of America Memoir 204, p. 85–98, https:// doi.org/10.1130/2009.1204(04).
- Hyndman, R.D., 2017, Lower-crustal flow and detachment in the North American Cordillera: A consequence of Cordillera-wide high temperatures: Geophysical Journal International, v. 209, p. 1779–1799, https://doi.org /10.1093/gji/ggx138.
- Jackson, S.E., Pearson, N.J., Griffin, W.L., and Belousova, E.A., 2004, The application of laser ablation-inductively coupled plasma-mass spectrometry to in situ U-Pb zircon geochronology: Chemical Geology, v. 211, p. 47–69, https://doi.org/10.1016/j.chemgeo.2004.06 .017.
- Janecke, S.U., 1994, Sedimentation and paleogeography of an Eocene to Oligocene rift zone, Idaho and Montana: Geological Society of America Bulletin, v. 106, p. 1083–1095, https://doi.org/10.1130/0016-7606(1994)106<1083:SAPOAE>2.3.CO;2.
- Janecke, S.U., 2007, Cenozoic extensional processes and tectonics in the northern Rocky Mountains: Southwest Montana and eastern Idaho: Northwest Geology, v. 36, p. 111–132.
- Janecke, S.U., and Blankenau, J., 2003, Extensional folds associated with Paleogene detachment faults in SE part of the Salmon basin: Northwest Geology, v. 32, p. 51–73.
- Janecke, S.U., and Snee, L.W., 1993, Timing and episodicity of middle Eocene volcanism and onset of conglomerate deposition, Idaho: The Journal of Geology, v. 101, p. 603–621, https://doi.org/10.1086/648252.
- Janecke, S.U., McIntosh, W., and Good, S., 1999, Testing models of rift basins: Structure and stratigraphy of an Eocene–Oligocene supradetachment basin, Muddy Creek half graben, south-west Montana: Testing supradetachment basin models: Basin Research, v. 11, p. 143–165, https://doi.org/10.1046/j.1365-2117.1999 .00092.x.
- Janecke, S.U., VanDenburg, C.J., Blankenau, J.J., and M'Gonigle, J.W., 2000, Long-distance longitudinal transport of gravel across the Cordilleran thrust belt of Montana and Idaho: Geology, v. 28, p. 439–442, https://

- doi.org/10.1130/0091-7613(2000)28<439:LLTOGA> 2.0.CO;2.
- Jicha, B.R., Singer, B.S., and Sobol, P., 2016, Re-evaluation of the ages of ⁴⁰Ar/³⁹Ar sanidine standards and supereruptions in the western U.S. using a Noblesse multicollector mass spectrometer: Chemical Geology, v. 431, p. 54–66, https://doi.org/10.1016/j.chemgeo.2016.03 024
- Ketcham, R.A., Gautheron, C., and Tassan-Got, L., 2011, Accounting for long alpha-particle stopping distances in (U-Th-Sm)/He geochronology: Refinement of the baseline case: Geochimica et Cosmochimica Acta, v. 75, p. 7779–7791, https://doi.org/10.1016/j.gca.2011 .10.011.
- Ketcham, R.A., Guenthner, W.R., and Reiners, P.W., 2013, Geometric analysis of radiation damage connectivity in zircon, and its implications for helium diffusion: The American Mineralogist, v. 98, p. 350–360, https://doi.org/10.2138/am.2013.4249.
- Kraus, M.J., 1985, Early Tertiary quartzite conglomerates of the Bighorn Basin and their significance for paleogeographic reconstruction of northwest Wyoming, in Flores, R.M., and Kaplan, S.S., eds., Cenozoic Paleogeography of the West-Central United States: Denver, Colorado, Rocky Mountain Section, Society of Economic Paleontologists and Mineralogists (SEPM), p. 71–91.
- Kuenzi, D.W., and Fields, R.W., 1971, Tertiary stratigraphy, structure, and geologic history, Jefferson Basin, Montana: Geological Society of America Bulletin, v. 82, p. 3373–3394, https://doi.org/10.1130 //0016-7606(1971)82[3373:TSSAGH]2.0.CO;2.
- Kuiper, K.F., Deino, A., Hilgen, F.J., Krijgsman, W., Renne, P.R., and Wijbrans, J.R., 2008, Synchronizing rock clocks of Earth history: Science, v. 320, p. 500–504, https://doi.org/10.1126/science.1154339.
- Leary, R.J., Smith, M.E., and Umhoefer, P., 2020, Grain-size control on detrital zircon cycloprovenance in the late Paleozoic Paradox and Eagle Basins, USA: Journal of Geophysical Research: Solid Earth, v. 125, https://doi.org/10.1029/2019JB019226.
- Lee, J.-Y., Marti, K., Severinghaus, J.P., Kawamura, K., Yoo, H.-S., Lee, J.B., and Kim, J.S., 2006, A redetermination of the isotopic abundances of atmospheric Ar: Geochimica et Cosmochimica Acta, v. 70, p. 4507–4512, https://doi.org/10.1016/j.gca.2006.06.1563.
- Link, P.K., Fanning, C.M., and Stroup, C.N., 2008, Detrital Zircon U-Pb Geochronologic Data for Selected Cretaceous, Paleogene, Neogene, and Holocene Sandstones and River Sands in Southwest Montana and East-Central Idaho: Montana Bureau of Mines and Geology Open-File Report 569, 5 p.
- Link, P.K., Stewart, E.D., Steel, T., Sherwin, J.-A., Hess, L.T., and McDonald, C., 2016, Detrital zircons in the Mesoproterozoic upper Belt Supergroup in the Pioneer, Beaverhead, and Lemhi Ranges, Montana and Idaho: The Big White arc, in MacLean, J.S., and Sears, J.W., eds., Belt Basin: Window to Mesoproterozoic Earth: Geological Society of America Special Paper 522, p. 163–183, https://doi.org/10.1130/2016.2522(07).
- Liu, L., and Stegman, D.R., 2011, Segmentation of the Farallon slab: Earth and Planetary Science Letters, v. 311, p. 1–10, https://doi.org/10.1016/j.epsl.2011.09.027.
- Liu, M., and Shen, Y., 1998, Crustal collapse, mantle upwelling, and Cenozoic extension in the North American Cordillera: Tectonics, v. 17, p. 311–321, https://doi.org/10.1029/98TC00313.
- Livaccari, R.F., 1991, Role of crustal thickening and extensional collapse in the tectonic evolution of the Sevier-Laramide orogeny, western United States: Geology, v. 19, p. 1104–1107, https://doi.org/10.1130/0091-7613(1991)019<1104:ROCTAE>2.3.CO;2.
- Lonn, J.D., McDonald, C., Lewis, R.S., Kalakay, T.J., O'Neill, J.M., Berg, R.B., and Hargrave, P., 2003, Geologic map of the Philipsburg 30' × 60' quadrangle, western Montana: Montana Bureau of Mines and Geology Open-File Report 483, 1 sheet, scale 1:100,000.
- Methner, K., 2016, Recovering Eocene paleotopography and paleoclimate of the North American Cordillera through integrated stable isotope and clumped isotope analyses [Ph.D. thesis]: Frankfurt, Germany, Goethe Universität Frankfurt/Main, 336 p.

- M'Gonigle, J.W., and Dalrymple, B.G., 1996, 40 Ar/39 Ar Ages of Some Challis Volcanic Group Rocks and the Initiation of Tertiary Sedimentary Basins in Southwestern Montana: U.S. Geological Survey Bulletin 2132, 17 p., https://doi.org/10.3133/b2132.
- Miall, A.D., 1977, Lithofacies types and vertical profile models in braided river deposits: A summary, in Miall, A.D., ed., Fluvial Sedimentology: Calgary, Alberta, Geological Survey of Canada, p. 597–604.
- Min, K., Mundil, R., Renne, P.R., and Ludwig, K.R., 2000, A test for systematic errors in 40Art/39Ar geochronology through comparison with U/Pb analysis of a 1.1-Ga rhyolite: Geochimica et Cosmochimica Acta, v. 64, p. 73– 98, https://doi.org/10.1016/S0016-7037(99)00204-5.
- Moye, F.J., 1988, Regional Geologic Setting and Volcanic Stratigraphy of the Challis Volcanic Field, Central Idaho: Idaho Geological Survey Bulletin 27, p. 87– 97, https://digitalgeology.aws.cose.isu.edu/Digital_ Geology_Idaho/papers/B-27ch01-4.pdf.
- Olsen, P.E., 1990, Tectonic, climatic, and biotic modulation of lacustrine ecosystems—Examples from Newark Supergroup of eastern North America, in Katz, B.J., ed., Lacustrine Basin Exploration: Case Studies and Modern Analogs: American Association of Petroleum Geologists Memoir 50, p. 209–224, https://doi.org/10 .1306/M50523C13.
- O'Neill, J.M., Lonn, J.D., Lageson, D.R., and Kunk, M.J., 2004, Early Tertiary Anaconda metamorphic core complex, southwestern Montana: Canadian Journal of Earth Sciences, v. 41, p. 63–72, https://doi.org/10.1139 /e03-086.
- Pardee, J.T., 1950, Late Cenozoic block faulting in western Montana: Geological Society of America Bulletin, v. 61, p. 359–406, https://doi.org/10.1130/0016-7606(1950)61[359:LCBFIW]2.0.CO;2.
- Parsons, T., 2006, The Basin and Range Province, in Olsen, K.H., ed., Continental Rifts: Evolution, Structure, Tectonics: Amsterdam, Elsevier, Developments in Geotectonics 25, p. 277–324, https://doi.org/10.1016 /S0419-0254(06)80015-7.
- Paton, C., Hellstrom, J., Paul, B., Woodhead, J., and Hergt, J., 2011, Iolite: Freeware for the visualisation and processing of mass spectrometric data: Journal of Analytical Atomic Spectrometry, v. 26, p. 2508–2518, https://doi .org/10.1039/c1ja10172b.
- Petrus, J.A., and Kamber, B.S., 2012, VizualAge: A novel approach to laser ablation ICP-MS U-Pb geochronology data reduction: Geostandards and Geoanalytical Research, v. 36, p. 247–270, https://doi.org/10.1111/j .1751-908X.2012.00158.x.
- Porter, R.C., van der Lee, S., and Whitmeyer, S.J., 2019, Synthesizing EarthScope data to constrain the thermal evolution of the continental U.S. lithosphere: Geosphere, v. 15, p. 1722–1737, https://doi.org/10.1130 /GES02000.1.
- Pujols, E.J., and Stockli, D.F., 2021, Zircon (U-Th)/(He-Pb) double-dating constraints on the interplay between thrust deformation and foreland basin architecture, Sevier foreland basin, Utah: Geosphere, v. 17, p. 1890– 1913, https://doi.org/10.1130/GES02372.1.
- Reiners, P.W., Farley, K.A., and Hickes, H.J., 2002, He diffusion and (U-Th)/He thermochronometry of zircon: Initial results from Fish Canyon Tuff and Gold Butte: Tectonophysics, v. 349, p. 297–308, https://doi.org/10.1016/S0040-1951(02)00058-6.
- Ronemus, C.B., Orme, D.A., Campbell, S., Black, S.R., and Cook, J., 2021, Mesoproterozoic–Early Cretaceous provenance and paleogeographic evolution of the Northern Rocky Mountains: Insights from the detrital zircon record of the Bridger Range, Montana,

- USA: Geological Society of America Bulletin, v. 133, p. 777–801, https://doi.org/10.1130/B35628.1.
- Rothfuss, J.L., Lielke, K., and Weislogel, A.L., 2012, Application of detrital zircon provenance in paleogeographic reconstruction of an intermontane basin system, Paleogene Renova Formation, southwest Montana, in Rasbury, E.T., Hemming, S.R., and Riggs, N.R., eds., Mineralogical and Geochemical Approaches to Provenance: Geological Society of America Special Paper 487, p. 63–95, https://doi.org/10.1130/2012.2487(04).
- Scarberry, K.C., Elliott, C.G., and Yakovlev, P.V., 2019, Geology of the Butte North 30' × 60' quadrangle, southwest Montana: Montana Bureau of Mines and Geology Open-File Report 715, 30 p., 1 sheet, scale 1:100,000.
- Scarberry, K.C., Yakovlev, P.V., and Schwartz, T.M., 2021, Mesozoic magmatism in Montana, in Metesh, J.J., and Vuke, S.M., eds., Geology of Montana, Volume 1—Geologic History: Montana Bureau of Mines and Geology Special Publication 122, 30 p.
- Schmandt, B., and Humphreys, E., 2011, Seismically imaged relict slab from the 55 Ma Siletzia accretion to the northwest United States: Geology, v. 39, p. 175–178, https://doi.org/10.1130/G31558.1.
- Schwartz, T.M., and Graham, S.A., 2017, Depositional history and provenance of Paleogene strata in the Sage Creek basin, southwestern Montana: Geosphere, v. 13, p. 1285–1309, https://doi.org/10.1130/GES01450.1.
- Schwartz, T.M., and Schwartz, R.K., 2013, Paleogene postcompressional intermontane basin evolution along the frontal Cordilleran fold-and-thrust belt of southwestern Montana: Geological Society of America Bulletin, v. 125, p. 961–984, https://doi.org/10.1130/B30766.1.
- Schwartz, T.M., Methner, K., Mulch, A., Graham, S.A., and Chamberlain, C.P., 2019, Paleogene topographic and climatic evolution of the Northern Rocky Mountains from integrated sedimentary and isotopic data: Geological Society of America Bulletin, v. 131, p. 1203–1223, https://doi.org/10.1130/B32068.1.
- Sharman, G.R., Sharman, J.P., and Sylvester, Z., 2018, detritalPy: A Python-based toolset for visualizing and analysing detrital geo-thermochronologic data: The Depositional Record: A Journal of Biological, Physical and Geochemical Sedimentary Processes, v. 4, p. 202–215, https://doi.org/10.1002/dep2.45.
- Simonsen, S., 1997, ⁴⁰Art/³⁹Ar ages of Eocene dikes and the age of extension in a Tertiary magmatic arc, Idaho and Montana [M.S. thesis]: Missoula, Montana, University of Montana, 121 p.
- Skelly, R.L., Bristow, C.S., and Ethridge, F.G., 2003, Architecture of channel-belt deposits in an aggrading shallow sandbed braided river: The lower Niobrara River, northeast Nebraska: Sedimentary Geology, v. 158, p. 249–270, https://doi.org/10.1016/S0037-0738(02)00313-5.
- Sláma, J., et al., 2008, Plešovice zircon—A new natural reference material for U–Pb and Hf isotopic microanalysis: Chemical Geology, v. 249, p. 1–35, https:// doi.org/10.1016/j.chemgeo.2007.11.005.
- Smith, M.E., Carroll, A.R., and Singer, B.S., 2008, Synoptic reconstruction of a major ancient lake system: Eocene Green River Formation, western United States: Geological Society of America Bulletin, v. 120, p. 54–84, https://doi.org/10.1130/B26073.1.
- Smith, M.E., Carroll, A.R., Jicha, B.R., Cassel, E.J., and Scott, J.J., 2014. Paleogeographic record of Eocene Farallon slab rollback beneath western North America: Geology, v. 42, p. 1039–1042, https://doi.org/10.1130 //G36025.1.
- Sonder, L.J., and Jones, C.H., 1999, Western United States extension: How the West was widened: Annual Review

- of Earth and Planetary Sciences, v. 27, p. 417–462, https://doi.org/10.1146/annurev.earth.27.1.417.
- Stockli, D.F., Surpless, B.E., Dumitru, T.A., and Farley, K.A., 2002, Thermochronological constraints on the timing and magnitude of Miocene and Pliocene extension in the central Wassuk Range, western Nevada: Tectonics, v. 21, https://doi.org/10.1029 /2001TC001295.
- Stroup, C.N., Link, P.K., Janecke, S.U., Fanning, C.M., and Yaxley, G.M., 2008, Eocene to Oligocene provenance and drainage in extensional basins of southwest Montana and east-central Idaho: Evidence from detrital zircon populations in the Renova Formation and equivalent strata: Arizona Geological Society Digest, v. 22, p. 529–546.
- Tänavsuu-Milkeviciene, K., and Sarg, F.J., 2012, Evolution of an organic-rich lake basin—Stratigraphy, climate and tectonics: Piceance Creek basin, Eocene Green River Formation: Sedimentology, v. 59, p. 1735–1768, https:// doi.org/10.1111/j.1365-3091.2012.01324.x.
- Vermeesch, P., 2021, Maximum depositional age estimation revisited: Geoscience Frontiers, v. 12, p. 843–850, https://doi.org/10.1016/j.gsf.2020.08.008.
- Vogl, J.J., Foster, D.A., Fanning, C.M., Kent, K.A., Rodgers, D.W., and Diedesch, T., 2012, Timing of extension in the Pioneer metamorphic core complex with implications for the spatial-temporal pattern of Cenozoic extension and exhumation in the northern U.S. Cordillera: Tectonics, v. 31, TC1008, https://doi.org/10.1029/2011TC002981.
- Vuke, S.M., 2020, The Eocene through early Miocene sedimentary record in western Montana, in Metesh, J.J., and Vuke, S.M., eds., Geology of Montana, Volume 1—Geologic History: Montana Bureau of Mines and Geology Special Publication 122, 38 p.
- Walker, R.G., and Cant, D.J., 1984, Sandy fluvial systems, in Walker, R.G., ed., Facies Models (second edition): Geoscience Canada Reprint Series 1, p. 71–89.
- Wells, R., Bukry, D., Friedman, R., Pyle, D., Duncan, R., Haeussler, P., and Wooden, J., 2014, Geologic history of Siletzia, a large igneous province in the Oregon and Washington Coast Range: Correlation to the geomagnetic polarity time scale and implications for a long-lived Yellowstone hotspot: Geosphere, v. 10, p. 692–719, https://doi.org/10.1130/GES01018.1.
- Westerhold, T., et al., 2020, An astronomically dated record of Earth's climate and its predictability over the last 66 million years: Science, v. 369, p. 1383–1387, https://doi.org/10.1126/science.aba6853.
- Whitney, D.L., Teyssier, C., Rey, P., and Buck, W.R., 2013, Continental and oceanic core complexes: Geological Society of America Bulletin, v. 125, p. 273–298, https:// doi.org/10.1130/B30754.1.
- Wolfe, M.R., and Stockli, D.F., 2010, Zircon (U-Th)/ He thermochronometry in the KTB drill hole, Germany, and its implications for bulk He diffusion kinetics in zircon: Earth and Planetary Science Letters, v. 295, p. 69–82, https://doi.org/10.1016/j.epsl.2010.03.025.
- Yonkee, A.W., and Weil, A.B., 2015, Tectonic evolution of the Sevier and Laramide belts within the North American Cordillera orogenic system: Earth-Science Reviews, v. 150, p. 531–593, https://doi.org/10.1016/j .earscirev.2015.08.001.

SCIENCE EDITOR: MIHAI DUCEA ASSOCIATE EDITOR: ROBINSON CECIL

Manuscript Received 20 July 2023 Revised Manuscript Received 28 October 2023 Manuscript Accepted 3 January 2024